3.2 THE GPM GV PROGRAM

Walter A. Petersen[1], Pierre E. Kirstetter[2], Jianxin Wang[3], David B. Wolff[4], Ali Tokay[5]

Abstract

We present a detailed overview of the structure and activities associated with the NASA-led ground-validation component of the NASA-JAXA Global Precipitation Measurement (GPM) mission. The overarching philosophy and approaches for NASA's GV program are presented with primary focus placed on aspects of direct validation and a summary of physical validation campaigns and results. We describe a spectrum of key instruments, methods, field campaigns and data products developed and used by NASA's GV team to verify GPM level-2 precipitation products in rain and snow. We describe the tools and analysis framework used to confirm that NASA's Level-1 science requirements for GPM are met by the GPM Core Observatory. Examples of routine validation activities related to verification of Integrated Multi-satellitE Retrievals for GPM (IMERG) products for two different regions of the globe (Korea and the U.S.) are provided, and a brief analysis related to IMERG performance in the extreme rainfall event associated with Hurricane Florence is discussed.

1.1.1 Overview

The overarching philosophy for NASA's implementation of GPM ground validation (GV) revolves around three highly complementary approaches (Hou et al., 2014; Skofronick-Jackson et al., 2017). These approaches include "direct", "physical" and "integrated" validation. Direct validation uses routinely available instrument networks and data products to assess convergence between and sources of uncertainty in GV ground- and GPM space-based precipitation estimates provided by the Dual-Frequency Precipitation Radar (DPR) and GPM Microwave Imager (GMI). Because versions of GPM products evolve as the mission progresses and statistical validation of orbital data should generally improve with the duration of sampling that occurs as the mission progresses, direct GV datasets are generally comprised of sustained data collections over regional to continental scales. As such, direct GV relies on contributions of high quality, calibrated ground observations from both operational and research instruments such as rain gauge and radar networks, regional and continental scale precipitation and hydrological products, and related activities on regional to continental scales.

[1] Walter A. Petersen
NASA Marshall Space Flight Center, Huntsville, AL, USA
e-mail: walt.petersen@nasa.gov
[2] Pierre-Emmanuel Kirstetter
Advanced Radar Research Center and School of Civil Engineering and Environmental Sciences, University of Oklahoma, Norman, Oklahoma, and NOAA/National Severe Storms Laboratory, Norman, Oklahoma, USA
e-mail: pierre.kirstetter@noaa.gov
[3] Jianxin Wang
Science Systems Applications International/NASA GSFC, Greenbelt, Maryland, USA
e-mail: jianxin.wang-1 @nasa.gov
[4] David B. Wolff
NASA Goddard Space Flight Center, Wallops Flight Facility, Wallops Island, VA, USA
e-mail: david.b.wolff@nasa.gov
[5] Ali Tokay
University of Maryland Baltimore County/NASA GSFC, Greenbelt, Maryland, USA
e-mail: ali.tokay-1 @nasa.gov

Physical validation operates within the larger envelope of direct validation, but is focused on the execution of field campaigns designed to study targeted precipitation processes for the testing and improvement of retrieval algorithms. This is accomplished by use of combined airborne and ground-based field measurements of cloud microphysical and precipitation properties through the atmospheric column. Common instruments used include airborne in situ cloud microphysical probes, high altitude airborne and ground-based mult-frequency and/or polarimetric radar, and airborne multi-frequency microwave radiometers spanning microwave frequencies sampled by instruments in the GPM satellite constellation. Field campaign observations are often further used for testing of coupled atmospheric simulations designed for active and passive microwave retrieval algorithm testing (e.g., Matsui et al., 2013). Finally, integrated validation is focused on the assessment and utility of GPM products and their uncertainties in hydrolometeorological and related applications. In a sense, integrated validation represents a bridge between GPM measurements, validation, and the hydrologic applications community.

Because many GPM applications and related "utilities" ultimately focus on quality of the products in a "direct" sense, in addition to outlining the NASA GPM GV program as a whole, this chapter will place a primary focus on relating GV datasets to direct validation activities with a brief review of results related to physical validation campaigns.

4.2.1.1 GV Measurement Synergy

NASA GV instrument components provide complementary precipitation measurements at a range of scales (Figure 1) in time and space. From a direct GV perspective, the requirement to validate myriad orbit-level GPM precipitation products (rain detection and intensity, drop size distribution, detection of snow etc.) at nearly instantaneous timescales for instrument fields of view (IFOV) of ~5 km or larger, requires the combined use of volume scanning multi-parameter radar and gauge instrumentation. From the perspective of physical GV (precipitation processes, algorithm physics) and integrated GV (hydrologic studies) sub-IFOV spatial scales are required.

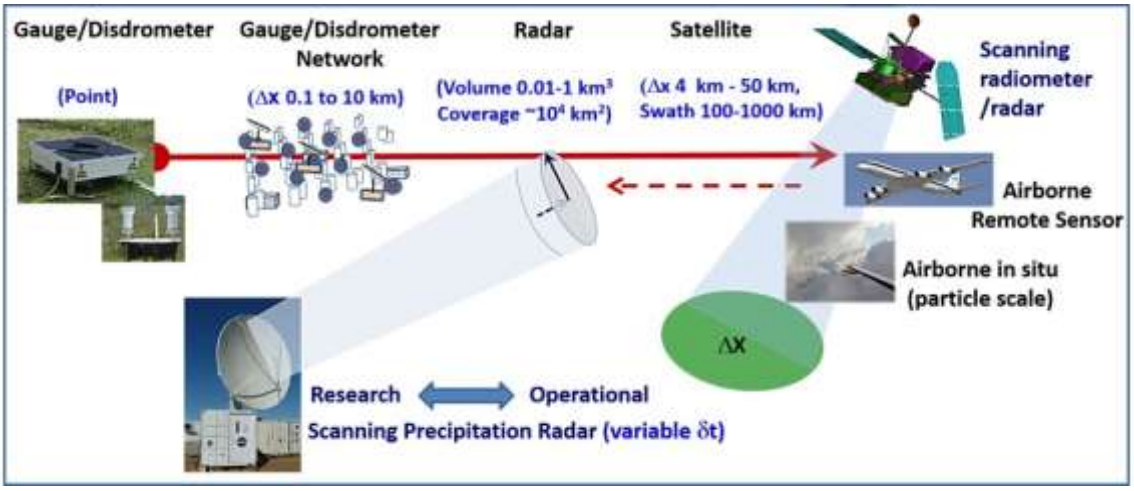

Figure 1. Translation of high quality precipitation measurements to satellite footprint and swath measurement scales for direct and physical validation.

Operating within and between the aforementioned scales and to accommodate the GV requirements, individual or spatially distributed rain gauge and disdrometer point measurements reference scanning dual polarimetric (DP) radar observations. In turn, DP radars translate the gauge and disdrometer measurements to instantaneously-viewed and spatially-distributed footprint, volume, and swath scales sampled by GPM satellite instruments. High quality national DP radar networks such as the WSR-88D radar network operated by the National Weather Service in the U.S., provide a continuous, reliable, and regional to continental scale "heartbeat" of statistical sampling, while research-grade DP

radars provide the capability to flexibly target 3-D precipitation structure from sub-footprint to regional scales at high space-time resolution. In turn, these ground observations support airborne in situ and remote sensing measurements collected during physical validation campaigns- a collective bridging of ground, atmospheric column and space-based measurements of the precipitation process.

4.2.2 Validation instruments, data, and examples

Herein we describe primary GV datasets with examples of direct GPM level-2 (individual orbit) DPR and GMI validation including GPM Core Observatory (hereafter, "GPM CO") "level-1" science requirements (L1SR; cf. Skofronick-Jackson et al., 2017). L1SRs can be summarized as follows: 1) quantify rainrates over the range [0.22-110] mm hr^{-1} ([0.2-60] mm hr^{-1}) and at effective resolution of 5 km (15 km) for DPR (GMI); 2) detect falling snow at the respective instrument effective resolutions for both DPR and GMI; 3) estimate rain rates at intensities of 1 mm hr^{-1} and 10 mm hr^{-1} within bias and uncertainty levels that do not exceed 50% and 25%, respectively, at a resolution of 50 km for the GPM CO; and 4) estimate the mass-weighted mean diameter (D_m) of the drop size distribution (DSD) to within +/-0.5 mm of GV measurements for DPR.

4.2.2.1 Primary datasets

U.S. and international GV datasets collected and routinely *processed* by the NASA GV team are summarized in Tables 1.1 and Table 1.2, respectively (see also Skofronick-Jackson et al., 2018).

Table 1.1: NASA GV primary U.S. data products routinely produced from GPM launch to present. Instruments at the WFF Supersite are often deployed for extended periods in targeted regimes or to augment external instrument networks of opportunity.

Product	Instrument	Data Product Description
U.S. Continental Scale/Multi-Regime Direct Validation		
GV Multi-Radar Multi-Sensor (MRMS) rain intensity and accumulation products	WSR-88D Radar and collective U.S. rain gauge networks	GV-processed CONUS NOAA MRMS (Zhang et al., 2016) radar/rain gauge bias-adjusted precipitation rates and types. Resolution of 2-minute and 0.01° x 0.01° for CONUS-coincident GPM orbits launch to present, and continuous 30 minute accumulations (cf. Kirstetter et al., this book)
Polarimetric Radar Validation Network (VN)	WSR-88D operational and Research grade (NPOL, KPOL) radars with GPM Satellite	For 70+ sites; CONUS/Offshore (including Kwajalein Atoll; KPOL) quality controlled DP radar and 3-D volumes of GPM Core satellite-coincident geo and volume-matched reflectivity, rain-rates, hydrometeor types, rain drop size distributions, and match statistics within 100 km range of ground radars.
NASA Wallops Super Site (WFF) Datasets		Supersite/instrument base established at WFF and the surrounding region. Coordinated, sustained collection of GPM satellite and GV overpass datasets.
Scanning S-band polarimetric radar volumetric precipitation characteristics	NASA NPOL S-Band Radar	GPM orbit-coincident/weather event PPIs, RHIs, vertically pointing volume scans (DP moments, hydrometeor types, rain rates, drop size distributions). 1° beam x 125 m range gates. (Gerlach and Petersen, 2012; Wolff et al., 2015)
Scanning dual-frequency (Ka/Ku) polarimetric radar volumetric precipitation characteristics	NASA Dual-frequency, Dual-pol. Doppler Radar (D3R)	GPM orbit-coincident/weather event PPIs, RHIs, vertically pointing volume scans and cross-sections (Ku/Ka-Band I&Q data, polarimetric moments, reflectivity, dual-frequency ratio, hydrometeor types, rain rates, drop size distributions). Radar ray 1° x 150 m range gates (Vega et al., 2014).
MRR-2/Pro precipitation profiles	K-Band Micro Rain Radar II/Pro	Continuous vertically pointing K-Band radar; 2° beam x 30 – 60 m resolution for 30 gates; reflectivity, velocity spectra, DSD, precipitation rate;
Disdrometer network hydrometeor size distributions, types, rain rate	2D-Video and Parsivel Disdrometers network	Disdrometer network continuous hydrometeor size distribution, types, shapes, and precipitation rates. 1–minute resolution, multi--instrument networks.
Precipitation imaging, rain and snow size distributions	Precipitation Imaging Package (PIP)	Continuous hydrometeor images, size distributions, fall-speeds, bulk density and water equivalent precipitation rate; deployments at WFF, Canada, Finland, Antarctica, Republic of Korea.
Dense rain gauge network rain intensity/accumulation	Single/dual/triple platform tipping bucket rain gauges	Continuous, quality-controlled, 1-minute average and accumulated rainfall, time of tip. 25 dual-platform gauges in network diameter of ~6 km, and numerous platforms in a broader 0.5° regional grid.
Snow, rain water accumulation rates	Pluvio 200, 400 weighing gauge network(s)	Continuous weighing-gauge frozen and liquid precipitation accumulations. Temporal scale 1 – 10 minute accumulations. Includes WFF, 12-gauge Marquette, Michigan network, international deployments.

These data are currently collected, or have been collected in an extended mode (one year or longer) for targeted continental and oceanic locations covering a variety of regimes, and from modes of near continuous continental scale monitoring to short-term periodic regional campaigns. Note that the international datasets shown in Table 1.2 represent only those data routinely processed by NASA

GPM GV; they do not represent the full complement of instrument, analysis, and product datasets collected by numerous international NASA Precipitation Measurement Mission (PMM) and GPM collaborating partners contributing to GPM GV around the globe (cf., Hou et al., 2014 and Skofrokick-Jackson et al. 2017). Many of these datasets can be accessed on the GPM GV website found at https://gpm-gv.gsfc.nasa.gov/.

Table 1.2: Routinely provided or extended international datasets processed by NASA GV including collaborative instrument deployments. WegenerNet- U. of Graz, Austria; CEMADEN- Brazilian Center for Natural Disaster Monitoring and Early Warnings; ECCC- Environment Climate Change Canada; FMI- Finish Meteorological Institute; KMA- Korean Meteorological Administration; KNMI- Royal Netherlands Meteorological Institute; Spain- U. of Castilla-La Mancha

Country	Product/Instrument Description
Austria	WegenerNet dense rain gauge network for GPM level-2 and IMERG footprint-scale validation (cf. Kirchenghast et al., 2014)
Brazil	CEMADEN; Routine/operational S-band dual-polarimetric radar volumes (9 radars) VN-processed; national rain gauge network
Canada	ECCC-deployed NASA PIP, Pluvio gauges and routine data collection at multi-instrument sites for snowfall studies
Finland	FMI/U. Helsinki C-Band polarimetric radar and supporting snow water equivelent data from NASA PIP, Pluvio, hot-plate instruments deployed at Hytiaala site for continuous collection of snow products (cf. von Lerber et al., 2018).
Republic of Korea	KMA hourly gauge-adjusted radar estimates (RAD-RAR) of rain accumulation for IMERG validation (see Suk et al., 2013)
Netherlands	KNMI C-band dual-pol radar data for VN processing
Spain-UCLM	UCLM-Toledo extended deployment of TREx dual-pol radar at NASA WFF site for coordinated multi-frequency radar scanning

We highlight for discussion three particular activities and associated datasets.

i) Validation Network (VN): A critical component of the direct validation strategy involves use of dual-polarimetric (DP) radar products (Fig. 1). More than 75 U.S. VN operational WSR-88D (land and ocean) and contributing international DP radars are used for statistical comparisons of VN equivalent radar reflectivity (Z_e), DP moments, and DP-derived precipitation parameters such as rain rate, the DSD (mass-weighted mean diameter, D_m, normalized intercept parameter, N_w), and hydrometeor types. VN databases are built by carefully geolocating and matching coincident VN and GPM DPR radar pulse volumes along all DPR rays (Schwaller and Morris, 2011). While the VN can be applied to virtually any DP radar and GPM overpass, the majority of VN radars used are located in the continental U.S. and were selected to minimize obvious radar quality issues associated with excessive beam blockage and clutter. As such, the majority of the VN radars used are National Weather Service WSR88-D DP radars located in the central to eastern continental U.S. Oceanic locations include DP radars in Kwajalein, Middleton Island, Hawaii, Guam, and Puerto Rico.
Specific to processing (cf. Pippitt et al., 2015), VN DP radar data first undergo quality control, and estimation of rain and hydrometeor properties. DP clutter removal, multiple radar rain rate estimators, DSD and hydrometeor identification algorithms are all applied using approaches well established in the literature. For example, precipitation estimates in VN radar volumes are accomplished using hybrid DP precipitation estimation approaches based various combinations of reflectivity (Z), differential phase (KDP), and differential reflectivity (ZDR) as summarized in Bringi et al. (2004), Cifelli et al. (2011), Chen et al. (2017), and Bucovcic et al. (2018). DSD retrievals derive from a heritage of radar modeling approaches of 2D Video Disdrometer (2DVD) data (e.g., Brandes et al., 2004; Thurai et al., 2012). The NASA GV team has collected 2DVD DSD datasets in a broad sample of precipitation regimes associated with locations of numerous physical-validation field efforts (Sec. 1.1.3) and extended multi-year observation periods at both Wallops Flight Facility (WFF) in Virginia and the Southeastern U.S. in Huntsville, Alabama. The 2DVD-diagnosed N_w and D_m are used to model polarimetric radar moments of Z and ZDR and create subsequent empirical functions relating the DSD observables to simulated ZDR and Z (e.g., Tokay et al., 2018). The derived equations for D_m [f(ZDR)] and N_w [f(Z,ZDR)] are then used with VN polarimetric data to generate volume fields of the DSD for ray and range gate comparisons to DPR observations. DP fuzzy hydrometeor idenfication algorithms (HID) are applied within the VN processing stream (e.g., Dolan and Rutledge, 2009 and references therein). After VN radar parameter retrievals are completed, GPM overpass and VN polarimetric data for precipitation events occurring within 100 km of a given radar are volume-

matched and compared at geometric intersections of the GPM DPR and ground radar scans (Bolen and Chandrasekar, 2003). To date, more than 45,000 volumes of coincident VN DP and GPM DPR radar data and derived products have been processed and matched since GPM launch. VN matched data files and intermediate DP radar and GPM data files are all archived.

ii) GV-Multi-Radar Multi-Sensor (MRMS) products: In parallel with the VN, NOAA/University of Oklahoma MRMS (cf., Zhang et al., 2016) radar-based estimates of precipitation are post-processed to provide a GPM GV dataset for continental scale statistical validation of GPM rain and falling snow water equivalent rates (SWER) over the U.S. (130W - 60W, 20N - 55N). It comprises precipitation rate and type (liquid, frozen, convective, stratiform) together with radar data quality and gauge-bias ratio metrics at 0.01° spatial resolution. The resultant product, termed Level-2 (L2) GV-MRMS, is suited to "instantaneous" orbit-level validation of GPM precipitation estimates for all CONUS GPM overpasses (Kirstetter et al. 2014). A 30-minute "level-3 (L3)" precipitation accumulation dataset (also including dominant precipitation type, radar data quality etc.) is also produced for validating products such as the GPM Integrated Merged GPM satellite rainfall product (IMERG; Tan et al., 2016, 2017, O and Kirstetter, 2018, Huffman et al., 2018).

The creation of a "best" GV-MRMS reference critically depends on additional adjustment and filtering of the datasets. For the GV-MRMS rain rate dataset, MRMS hourly gauge-bias adjustments are applied to 2-minute radar-estimated rain rates using a spatially-variable multiplicative bias field (e.g., Amitai et al., 2012, Kirstetter et al., 2012). A conservative filtering is applied on instances when the radar and gauge have significant quantitative disagreement (i.e., radar–rain gauge hourly ratios outside of the range 0.1–10) and by using a radar quality index (RQI). Only GV-MRMS rain pixels associated with RQI values of 1.0 are used to validate GPM rain rates. Snow water equivalent rates (SWER) (cf. Zhang et al, 2016) are processed at the same temporal/spatial scales as rain but with no bias correction or RQI-based filter applied, instead, additional beam height filters are used (cf. Sec. 4.2.2.4). Use of GV-MRMS data is constrained to a large region of CONUS where beam heights are $\leq$ 2km (1.5 km) for rain (snow) for evaluating L1SR near surface precipitation rate criteria.

While the filtering approaches mentioned may not eliminate all errors in the GV-MRMS reference, they standardize the reference product across regions of the U.S. The evaluation of MRMS rain rates at fine scale (0.01° and 5-km) by Kirstetter et al. (2015) demonstrated that biases are significantly mitigated using these qualitative and quantitative filtering procedures. Additional evaluation of the GV-MRMS using spatially-dense NASA WFF Pocomoke and Nassawadox rain gauge networks (Table 1.1) demonstrated GV-MRMS biases of 10%-15% or less and random errors of 35-40 % for hourly rain rate estimates at the nominal footprint of the DPR. For L1SR verification we assume that the MRMS bias relative to that observed with the dense GV gauge networks will remain at or below ~15% at the 50 km scale, and that random errors will substantially decrease with spatial averaging (e.g., Steiner et al., 2003). For GPM L1SRs related to detection of snow, initial evaluations of MRMS rain/snow delineation are favorable, though cases of weak horizontal temperature gradients can be challenging (Chen et al. 2016). The high spatial resolution of GV-MRMS allows matching the resolution of any L2 and L3 GPM precipitation and estimate area-mean precipitation rates along with sub-IFOV precipitation occurence, variabilty and types for direct validation of GPM DPR, GPROF, and IMERG products (Kirstetter et al. 2012, 2014, 2015; Tan et al., 2016, 2017a, Kidd et al., 2018).

iii) NASA WFF GV Precipitation Research Facility Products and Support Activities: GPM GV maintains a world-class instrumentation network based at the NASA Wallops Flight Facility (WFF) on the mid-Atlantic Eastern Shore of Virginia. Instruments operated as part of this "supersite" include NASA's S-band DP radar (NPOL; Gerlach and Petersen, 2011; Wolff et al., 2015), the Ku-Ka band Dual-frequency Dual-Polarimetric Doppler Radar (D3R; Vega et al., 2014), Micro Rain Radars (MRR-2, MRR-Pro), Precipitation Imaging Package(s) (PIP; e.g, Newman et al 2009; von Lerber et al., 2018), Pluvio-2 weighing gauges, and networks of multi-tipping bucket rain gauge platforms and disdrometers (2D Video, Parsivel).

NPOL radar data are quality controlled and and used for GPM direct statistical and physical process studies by science team members. D3R datasets are stored in raw I&Q form and further processed on a case-by-case basis by team members at Colorado State University. D3R data products include attenuation corrected Ku/Ka-band reflectivity, derived quantities such as rain rates, hydrometeor types and DSD. When not deployed for field campaigns, the instruments are operated within the WFF network (or other domestic partner sites) to collect data during GPM overpasses and other weather-related targets of opportunity. Subsets of these instruments are also routinely operated with international GV partners (Table 1.2). WFF rain gauge network datasets are quality controlled and processed to create time-of-tip and one-minute splined rain rate products (e.g., Wang et al., 2008). The products are used to estimate area-mean rain rate at footprint scales and compile intrafootprint variabilty statistics, as an independent means of verifying GV-MRMS rain rate estimates (e.g., Marks et al., 2017), and direct validation of GPM DPR, GPROF, and IMERG products (Tan et al., 2016, 2017b, Kidd et al., 2018). Disdrometer network data (2D Video, Parsivel) are used for verifying GV radar calibration, developing DSD retrieval algorithms for GV polarimetric radars in the course of evaluating GPM DSD science requirements, and for studies of global to footprint scale DSD variability (Williams et al., 2014, Liao et al., 2014, Gatlin et al., 2015, Bringi et al., 2015, Thurai et al., 2017, Tokay et al, 2017).
For snow, PIP data are used to quantify the snow particle size distribution, bulk density, and to verify GV SWER products (e.g., Huang et al,. 2015, Kniefel et al., 2015, von Lerber et al., 2018). Liao et al. (2016) used WFF PIP data to demonstrate GPM DPR dual-frequency ratio application to retrievals of bulk snow water contents and equivalent rates independent of derived particle size distribution parameters.

4.2.2.2 Example Applications of VN datasets

VN datasets serve as a check on satellite and ground-based radar calibration, algorithm performance, and derived parameter stability between GPM product versions. Figure 2 illustrates one example- VN detection of the DPR reflectivity calibration change that occurred with release of DPR Version 5 (V5) products. In Figure 2, VN and DPR sample volumes are compared for stratiform precipitation observed above the melting layer. Interestingly, the DPR reflectivity shift also impacted retrieved parameters such as D_m (Figure 3), evident as a slight (~0.2 mm) shift in the bias between V4 and V5 D_m relative to VN. Figure 3 also demonstrates that the GPM retrieval of D_m satisfies L1SRs.

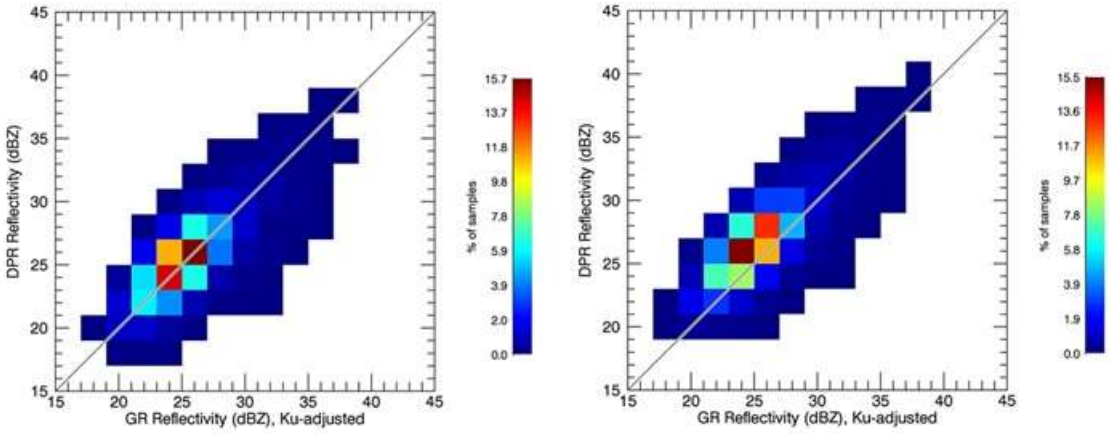

Figure 2. VN verification of DPR calibration adjustment. The DPR Ku-band radar calibration was adjusted by JAXA from Version 4 (V4; left) to Version 5 (V5; right). The V5 increase of DPR Ku-Band radar reflectivity (Z_e) by ~1.2 dB (y-axis) is clearly evident in relative frequency histograms (shaded, percent) when plotted against the Ku-adjusted VN Z_e (GR: X-axis).

Another example for application of the VN includes direct verification of DPR algorithm corrections of Path Integrated Attenuation (PIA) as a function of precipitation type (e.g., convective/stratiform). Indeed, PIA-corrected reflectivity as a function of precipitation type is fundamental to DPR precipitation estimation and DSD retrieval (e.g., Seto and Iguchi, 2015). The correction of DPR reflectivity and subsequent retreival of precipitation rates can be especially challenging for convective precipitation at the frequencies used by the DPR. However, the VN data provide a robust verification of GPM PIA algorithm ability to correct convective reflectivity profiles (e.g., Fig. 4).

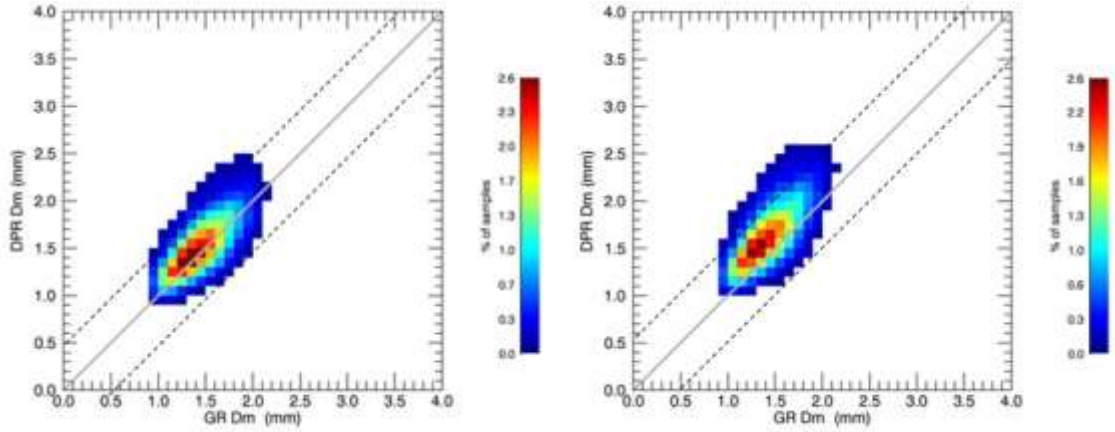

Figure 3. As in Fig. 1, but D_m (mm). Displayed are the V4 (left) and V5 (right) DPR D_m relative to GV. Adjusting the DPR calibration in V5 resulted in a slight, but perceptable positive bias shift in the DPR D_m relative to GV. NASA L1SRs for D_m (+/- 0.5 mm) indicated by dashed lines.

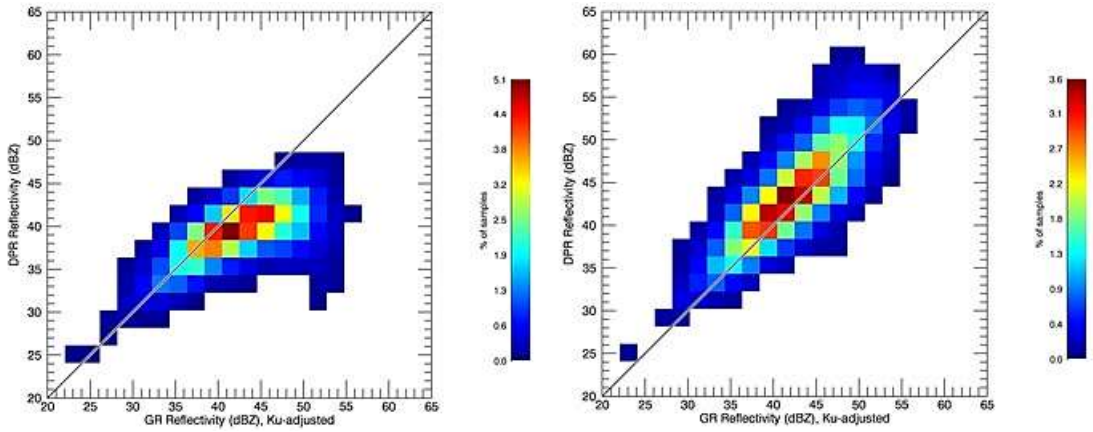

Figure 4. DPR Measured (left) and PIA-corrected (right) V5 Ku-Band radar reflectivity (y-axis) in convective precipitation plotted against VN radar reflectivity (x-axis) for layers of precipitation below the height of the 0°C level. Similar results are attained for stratiform precipitation (not shown).

More recently we have been modifying the VN for direct validation of GPM SWER. The approach recognizes the intrinsic difficulties in measuring an instantaneous SWER (even at the ground) at IFOV scales. The methodology relies on multiple radar-based estimators, seeking only first-order agreement between the DPR and the VN estimates. We leverage VN DP radar hydrometeor HID fields to identify the occurrence of snow and then estimate SWER using polarimetric estimators (e.g., capturing physical variabilty in the SWER; Bukovcic et al., 2018), or reflectivity-SWER (Z-S) equations based on probabablistic quantitative precipitation estimation (PQPE; e.g., Kirstetter et al., 2015). The VN estimation "ensemble" is thus constructed from a single DP estimator, and three PQPE estimators (representing the 25th, 50th, and 75th percentile of Z-S SWER relationships). Verification of VN SWERs (Figure 5) is being tested against 11 Pluvio snow-gauges deployed in~15 km footprint located over and to the southwest of the Marquette, Michigan WSR-88D radar.

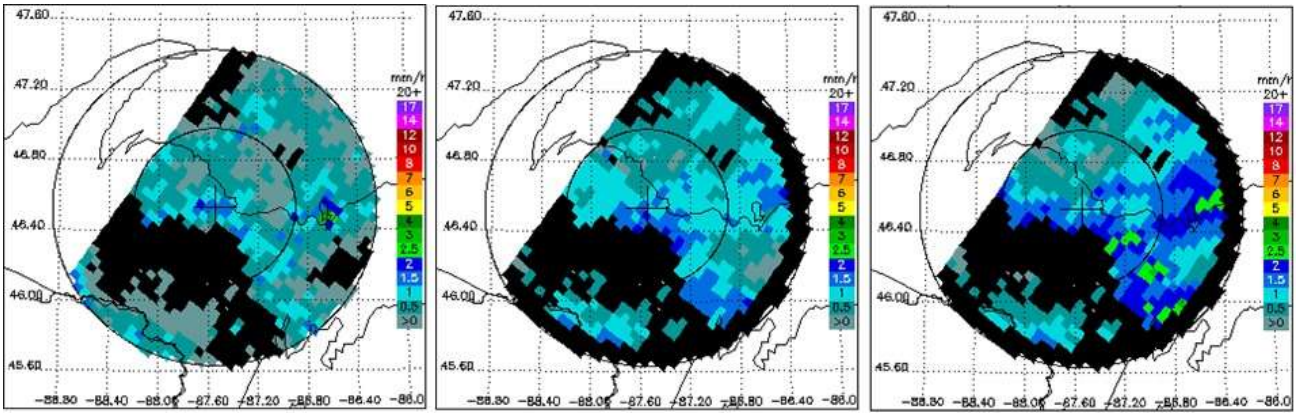

Figure 5. Coincident and DPR footprint-matched VN-estimated SWER using the Marquette, Michigan WSR-88D radar (KMQT) and Pluvio network in the DPR swath, April 15, 2018. The DPR single frequency estimate (left) is compared against the DP radar (center) and PQPE median estimators (right). The MQT Pluvio network is located west through south of KMQT and within 15 km range. Range rings are illustrated at 50 and 100 km from KMQT.

Preliminary results (Figure 5) indicate that the DPR estimates generally fall within the bounds of the VN estimators (all within a factor of two on SWER). Pluvio network reference data (20-minute mean and median SWER) for the 15 km footprint indicate a mean SWER of 2.4 mm hr^{-1}, with an individual gauge range of 1.4-3.3 mm hr^{-1}. Of the VN radar estimates, the PQPE median (50th percentile) estimator was the highest, with the DP radar estimator providing the best match to the Pluvio estimates. The DPR estimate was slightly lower than the VN DP estimator. When upscaled to the CONUS-wide VN network for the full winter of 2018 (Figure 6), a similar trend is found. That is, the DPR markedly underestimates the 50th percentile PQPE SWER but more closely resembles the DP SWER and even the 25th% PQPE SWER. Further verification of the VN estimators using the Pluvio network and other select measurement sites will enable more quantitative estimation of the uncertainty in VN SWER estimates resulting in improved application to GPM validation efforts.

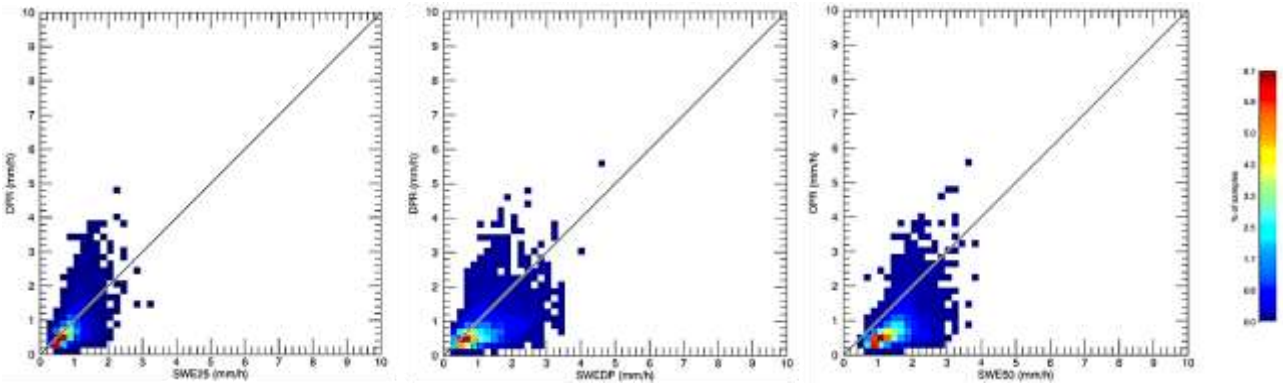

Figure 6. Scatter density plots for winter 2017/18 DPR normal swath (y-axis) SWER plotted against VN-estimated SWER (x-axis) for the PQPE 25th % (left), dual-pol (center), and 50th % (right) SWER estimators. It is clear that the DPR SWER estimate best matches the VN dual-polarimetric SWER.

4.2.2.3 Validation using GV-MRMS

In parallel with VN datasets, high resolution GV-MRMS data serve as the primary contiguous continental scale reference for verifying GPM near surface rain rate estimation and snowfall detection. The data provide an efficient and statistically robust means to evaluate IFOV behavior of DPR estimates of rain rate for individual algorithm versions, precipitation regimes and types, and to

monitor evolution of algorithm versions as the mission progresses. Relative to evaluating the overall quality and evolution of the DPR retrievals using the GV-MRM, consider Figures 7 and 8. Both figures provide scatter density plots for different radar-based retrieval algorithms. For example, data shown in the single frequency KuPR algorithm scatter plots of Figure 7 suggest reasonable but somewhat similar comparisons between KuPR and the GV-MRMS across V4 to V6. The net relative bias behavior in the Ku-PR estimate relative to GV-MRMS for all rain types evolves from a value of +2% in V4 to -10% in V5, with correlations of 0.53 to 0.51, respectively. Alternatively, in Figure 8, GV-MRMS products indicate that GPM rain rates estimated using the combined dual-frequency capability of the DPR radar and the GMI radiometer (e.g., the combined-radar radiometer algorithm; Grecu et al., 2016) more clearly improve with versions. A much better match to the GV-MRMS is evident in V5 and V6 relative to V4, with a relatively large V4 sample bias of +61% that markely decreases to -3.6% in V5, and is +5.8% V6. Correlations were similar between versions at 0.59, 0.55 and 0.56 for V4, V5 and V6 respectively.

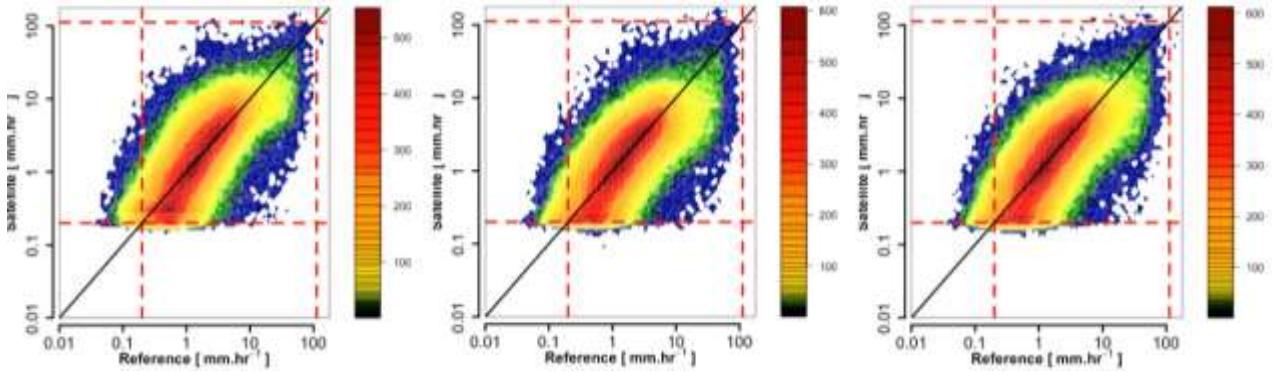

Figure 7. Evolution of GPM versions. Joint histograms of GV-MRMS reference rain rate (x-axis) for all rain types plotted against matched DPR 2AKu-algorithm IVOV rain rate estimates (y-axis) V4 (left), V5 (center) and V6 (right).

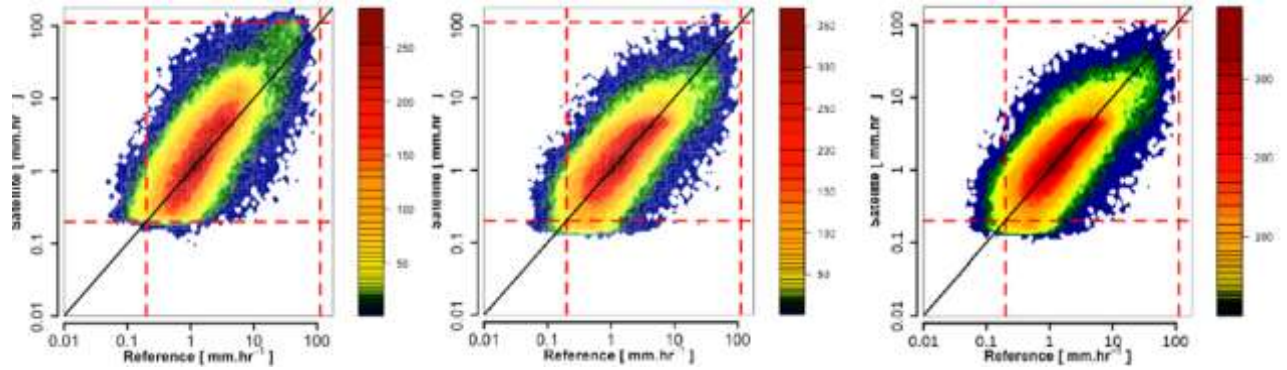

Figure 8. As in Fig. 7, but matched-swath dual-frequency combined radar-radiometer algorithm.

Importantly, the data points in Figures 7 and 8 are dominated by the occurrence of stratiform precipitation (e.g., rates typically below 10 mm hr^{-1}). It is therefore interesting to examine the same data points partitioned as a function of their convective (C) or stratiform (S) rain rate classification (e.g., Figure 9). Figure 9 displays the C and S precipitation comparisons for the combined algorithm, but the same behavior is also observed in the KuPR product. Also, recall from the VN example shown in Figure 4 that the retrieval algorithm does a reasonable job of correcting the radar reflectivity in convection. In Figure 9, the stratiform rain rate scatter is reasonably well behaved, resembling that of Figure 8. However, the convective rain rates of the GPM combined algorithm exhibit more error relative to the GV-MRMS, most notably at higher (> 5 mm hr^{-1}) and lower (< 1 mm hr^{-1}) rain rates. These departures from the GV-MRMS in convective rain contribute to the trends in Figures 7 and 8, but the underlying behavior is masked.

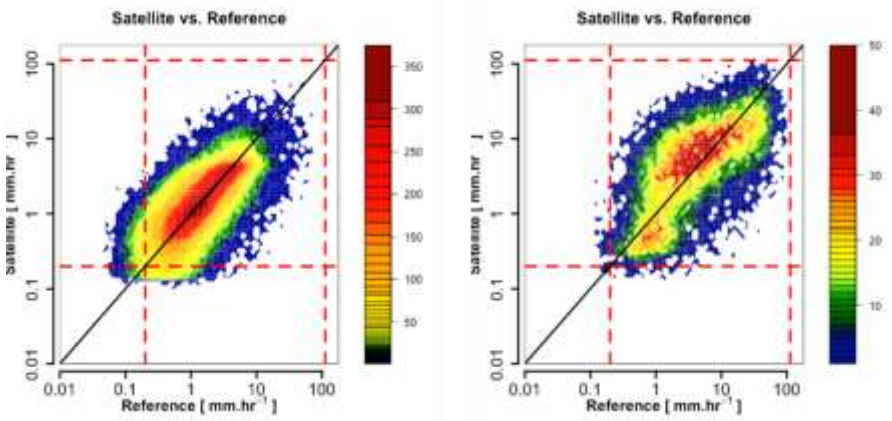

Figure 9. As in Figure 8, but V5 combined algorithm for stratiform (left) and convective (right) precipitation. The KuPR algorithm strongly resembles this plot as well.

Behavior in the DPR-derived rain rates is important to track as they serve as an a priori database for radiometer retrievals in the Goddard Profiling (GPROF) algorithm (Kummerow et al., 2015). Consider Figure 10 which displays gridded comparisons of the KuPR and GMI-GPROF rain estimates over the continental U.S. to the GV-MRMS product. The KuPR product compares well to the GV-MRMS, but is most notably high biased (on average 25-30%) in the southern and central mid-section of the U.S. In tandem, the GPROF product also displays a high bias, though more pronounced, in the mid-section of the U.S. Conversely, over the eastern seaboard and neighboring Appalachian region, the GPROF is slightly lower than the GV-MRMS.

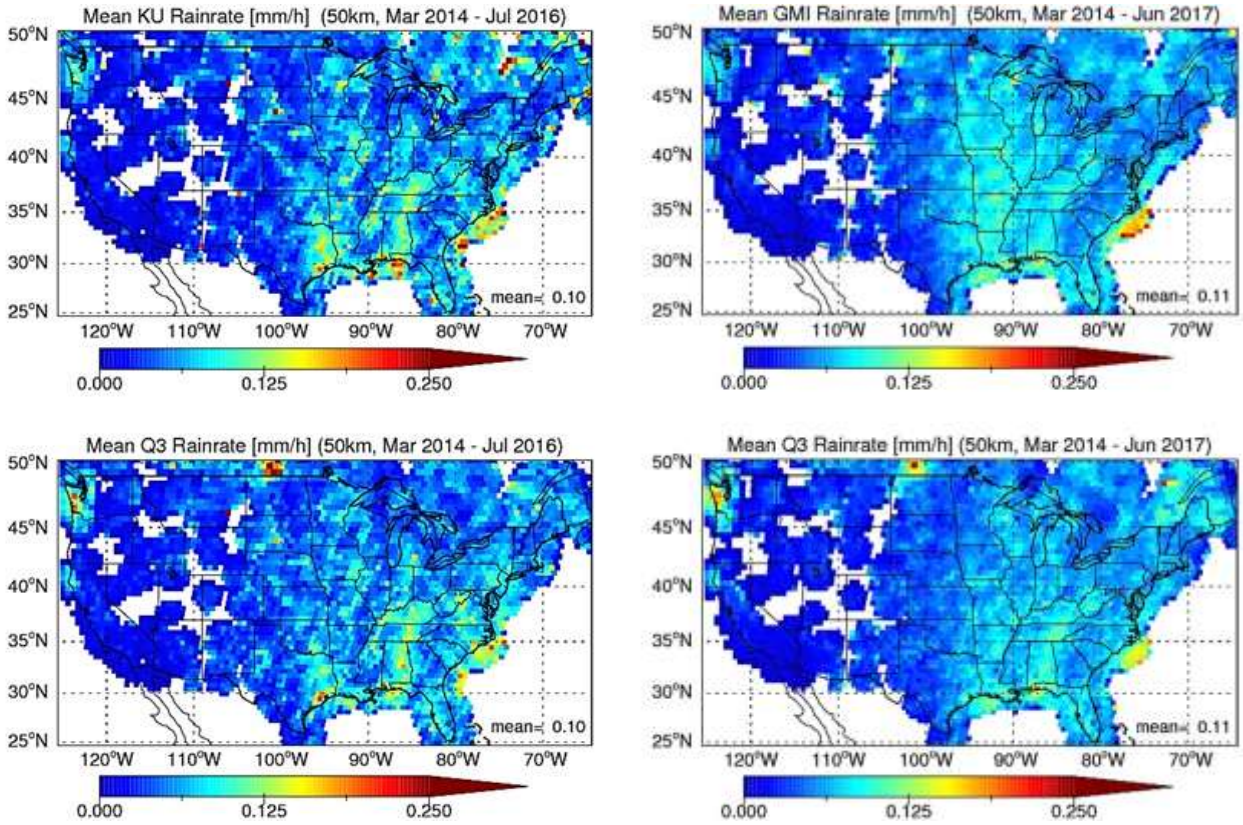

Figure 10. KuPR (top left) and GMI-GPROF (top right) 50 km gridded mean rate rates (mm hr^{-1}) plotted against their matched sample of GV-MRMS (indicated as "Q3") rain rates in bottom panels. While GPROF precipitation estimates over land do rely on DPR-retrieved precipitation profiles, the attribution of error in GPROF rain rate is complicated. This is because the algorithm is intrinsically

related to underlying ice-scattering relationships to rainfall, land surface emission characteristics, forecast model analysis error and bias in relation to environment state, and even potential GV-MRMS matchup errors associated with parallax assumptions (e.g., Guilloteau et al. 2018). As is evident in Figure 10 (contrast behavior in the west to that of the central U.S.) the aforementioned rain and surface characteristics shift with geography (see also Kidd et al., 2018), and these are also likely tied to precipitation type/regime. On the other hand, understanding something about the underlying state of a given environment that supports a given rainfall regime can be used to improve the algorithm (e.g., Petkovic and Kummerow, 2017).

4.2.2.4 Application to verification of GPM L1SRs

As discussed previously, NASA's GPM L1SRs (Sec. 1.1.2; Skofronick-Jackson et al., 2017) define specific measurement range and error standards for retrieved precipitation parameters such as rain rate and raindrop size distribution, and somewhat more binary requirements for the detection falling snow (as opposed to estimation of water equivalent rate). Figures 3 and 5-8, while used to illustrate GV monitoring of the evolution of GPM product versions or evaluation of SWER, also provide robust examples of L1SR verification of GPM L2 products. As noted previously, Fig. 3 illustrates satisfaction of the GPM L1SR pertaining to D_m estimation sing VN GV data (Tokay et al., 2018). GV-MRMS data in Figs (6-8) confirm L1SR rain rate intensity ranges sampled at IFOV scales (e.g., 5 km for the DPR, 15 km GMI- not shown) and consistency between GPM product versions.
Figure 10 provides one example of GV-MRMS product use for examining bias and uncertainty errors between GV and GPM over CONUS for L1SR grid scales (50 km). Note that these maps are continuously updated as GV-MRMS datasets and GPM CO level-2 data are produced and downloaded and as GPM versions change. For the formal verification process for L1SRs, we conservatively selected a large sub-region of the central and southern Plains of the U.S. where GV-MRMS beam heights and rain gauge density requirements were optimal. A comparison for this region is exhibited in Figure 11 for the GPM V6 Combined Dual-Frequency Radar-Radiometer algorithm. As illustrated in Skofronick-Jackson et al. (2018) for V5, V6 also easily meets L1SRs over the CONUS region sampled.

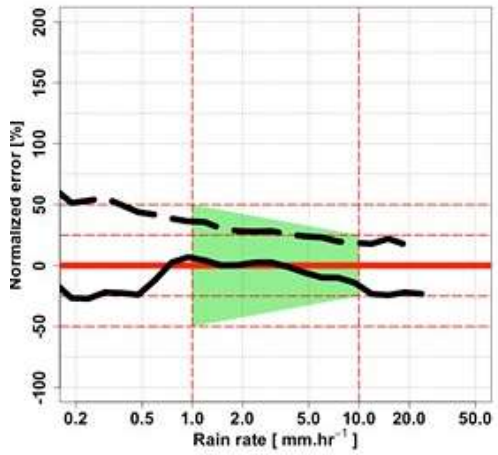

Figure 11. GPM V6 combined radar-radiometer algorithm matched-swath rain rates (x-axis) vs. normalized error (%; y-axis) at 50 km grid scales over the CONUS L1SR region. Solid line is relative bias, dashed line is NMAE. Green shading represents L1SR requirement (cf. Skofronick-Jackson et al. 2018 for V5 result).

As in Figure 9, Figure 11 shows a low bias (25%) for rain rates on the convective (> 5-10 mm hr^{-1}) and light rain ends (<0.6 mm hr-1) of the rain rate spectrum. Though under investigation at this time, candidate explanations for the low biases include a combination of impacts ranging from approaches to constrain the DSD in the algorithms (e.g., Grecu et al., 2016), non-uniform beam filling and/or possible multiple scattering impacts on correction of path integrated attenuation, related DSD biases observed in convective rain (e.g., Petersen et al., 2018), or incorrect assumptions about the functional form of the DSD applied at the light rain rate end of the spectrum (e.g., Thurai et al., 2017).
In addition to comparisons reported for the CONUS (over land), we have also tested L1SRs over the ocean (e.g., Fig. 12). Here we selected two oceanic dual-polarimetric radar sites representing distinctly different regime types; i.e., tropical and mid/high-latitude climates. The radars and sites included the Kwajalein Atoll dual-pol (K-pol) radar operated by the U.S. Army (with a strong tradition of GV use during the NASA TRMM era; e.g., Marks et al., 2011), and the WSR-88D radar

located on Middleton Island, Alaska (PAIH). Both radars were selected for their relatively open view of the ocean at ranges of 100 km or greater. Internal polarimetric consistency checks (cf. Marks et al, 2011), calibration adjustments (Wolff et al., 2015), and VN matched-volume comparisons of radar reflectivity between K-Pol, and GPM were used intermittently to monitor, verify and if necessary correct the reflectivity calibration on both platforms.

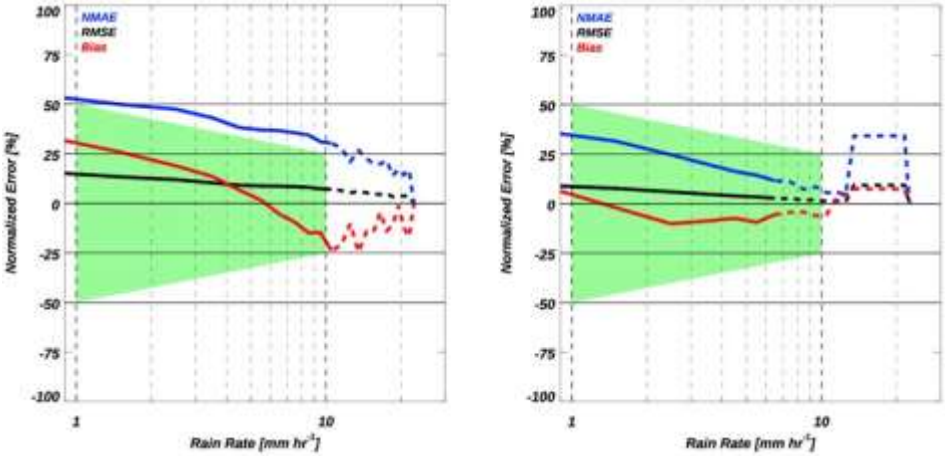

Figure 12. Similar to Figure 11 but for instrument footprint scales in the Kwajalein (K-pol; left), and PAIH (right) oceanic domains. The red line represents bias (%) and the blue line indicates normalized mean absolute error (NMAE; %) at EFOV scales. The solid black line indicates the RMSE (%) for EFOVs scaled to 50 km using Steiner et al. 2003.

The quality-controlled data were subsequently interpolated to a 1 km Cartesian grid, with gridded rain rate files containing rain estimates based on the aforementioned DP radar retrieval methods (Cifelli et al. 2011 used for Fig. 12). In contrast to Figure 12 and use of GV-MRMS over CONUS, because the number of 50 x 50 km grid boxes in a single 100 km radar–range domain is fairly limited. Hence, to demonstrate verification of L1SRs we use matched GV radar - GPM IFOVs. For each GPM overpass of a given site, the GV radar volume scan occurring closest in time to each overpass was identified and 1-km gridded rain rates at the 1 km height level located in each IFOV pixel were averaged. For the collection of matched pixels we then calculated the bias, root mean square error (RMSE), mean absolute error, and NMAE. To evaluate L1SR criteria we assumed that the bias computed at the IFOV scale does not increase at 50 km grid scales, that the L1SR uncertainties could be computed using RMSE computed for IFOV scales and scale-adjusted via Steiner et al., (2003).
An example is shown in Figure 12 for the combined radar-radiometer algorithm matched-swath (MS) product. The quality of the combined radar-radiometer algorithm meets L1SRs for estimation of the rain rate in both of the contrasting oceanic rain regimes. However, there are differences in behavior between bias and uncertainty trends of the tropical and mid-latitude regimes of Figure 12, and similarly between the oceanic regimes and land regime sampled in Fig. 11. Considered with Figure 10, these differences emphasize the non-global nature of rain rate retrieval errors in relation to the convergence of ground and space-based estimates of rainfall (cf. Kidd et al., 2018).
In addition to rain rate and DSD, L1SRs also require that GPM CO instruments demonstrate "detection" of snow at GPM CO instrument IFOVs. Demonstration that GPM meets this L1SR has been accomplished several ways. For example, we can directly compare ground-identified occurrences of snowfall coincident with satellite IFOVs (e.g., Figs. 5-6; see also von Lerber et al., 2018). We can also use larger datasets such as the GV-MRMS to statistically determine the delineation of snow from rain when precipitation is detected by the GV-MRMS and the CO. Additionally, we can attempt to identify a lower GV-MRMS snow water equivalent rate (SWER) threshold defining the satellite detection capabilities. For the latter two tests the Heidke Skill Score (HSS) has proven useful for managing the tradeoff between increasing the percentage of correct detections (snow versus rain for delineation, positive versus zero snow rate for detection) and

minimizing misses. An HSS value of one (zero) indicates perfect (no) contingency skill. For GPM L1SRs, when considering the delineation of snow from rain computation of the maximum HSS suggests reasonable performance at values of ~0.65 and ~0.47 for the DPR and GMI, respectively. For evaluating the "detection" of snow as a function of estimated water-equivalent snowfall rate, the HSS is computed as a function of the detected reference water-equivalent rate (based on a Z-S of $Z = 75*S^2$, random error suspected to be large). Maximizing the HSS enables us to identify the approximate lower threshold SWER for snow detection and to evaluate this model. Using this approach the maximum HSS=0.65 for the CO and occurs at a water equivalent rate of 0.53 mm hr^{-1} for the DPR MS product. The maximum HSS for the GPROF GMI product is 0.34 at a rate of ~0.6 mm hr^{-1}. Both DPR and GMI GPROF HSS appear to exhibit some very limited skill down to an SWER of ~0.3 mm hr^{-1}. Interestingly, the HSS-based SWER threshold values of 0.5 to 0.6 mm hr^{-1} for the GMI are similar to those computed in previous theoretical work conducted by Skofronick-Jackson et al. (2013). You et al. (2016) presented probability of detection results for the GMI that are consistent with our results- demonstrating GMI radiometer detection capability maximized by use of the higher frequency 166 GHz channel. Though numerous ways exist to approach the problem, GPM satisfies its L1SR for snow detection.

4.2.3 Physical Validation Activities

Physical validation (PV) datasets originate from a plethora of pre and post-launch GPM GV field campaigns (Table 1.3). Data to validate retrieval algorithm assumptions and methodologies have been collected for a range of precipitation regimes and types. In the broadest sense PV data necessarily include most, if not all of the ground-based direct-statistical datasets discussed above (including processing), for both rain and snow regimes, with the important distinction that almost all PV datasets (except WFF, the Iowa Flood Studies campaign) also include high-altitude airborne (ER-2, DC-8) remote sensing data, airborne microphysical measurements, and supporting sounding profiles of atmospheric thermodynamic state (e.g., Skofronick-Jackson et al., 2015, Jensen et al., 2016, Houze et al. 2017). Airborne remote sensing datasets collected in PV campaigns serve as "proxy GPM satellite measurements" and depending on the siutation, were coordinated with GPM overpasses when possible. The PV datasets generally include coincident downward looking multi-frequency radar collections at all or several of W, Ka, Ku, and X-band frequencies, and passive microwave radiometer data covering the 10-183 GHz frequency ranges. In situ airborne microphysical data were collected in coordination with remote sensing and ground-based instruments and used standard suites of microphysical probes that span measurement scales of aerosol (0.1 μm) to large hydrometeors (2 cm). Airborne and ground-based PV data have supported a variety of algorithm applications related to the physics and spatial variability of rain DSDs (e.g., Williams et al., 2014, Liao et al. 2014, Bringi et al., 2015, Gatlin et al., 2015, Thurai et al., 2017, Zagrodnik et al., 2018, Tokay et al., 2017, 2018) to include regime variability (Dolan et al. 2018), radar multiple-scattering and detection of the multiple scattering "knee" at DPR frequencies in strong convection (Heymsfield et al., 2014; Battaglia et al., 2014, 2016), ice hydrometeor profiles and radiometer response (Leppert et al., 2015), and ice and snow scattering at multiple radar frequencies (Molthan and Petersen, 2011, Olson et al., 2014, Kneifel et al, 2015; Chase et al., 2018; Leinon et al. 2018). PV datasets have also supported development of new GV methods for radar calibration (Wolff et al., 2015, Louf et al., 2018), creation of multi-parameter rain rate reference products (Seo et al., 2018), and multi-dataset fusion and analysis (e.g., Wingo et al., 2018). New analyses relative to snowfall estimation include reference estimation of bulk snow density and snow water equivalent rates (e.g., Huang et al., 2015, von Lerber et al., 2018) and the potential limitations of snow water equivalent rate estimation using passive microwave (Skofronik-Jackson et al., 2013). Finally, the field data have supported tests of cloud resolving model physics (e.g., Tao et al., 2013; Lang et al., 2014, Iguchi et al, 2014, Tao et al., 2016, Colle et al., 2017), and column microphysical impacts on satellite remote sensing simulators (Matsui et al., 2013).

Data from GPM PV campaigns are archived at the NASA Global Hydrology Resource Center (GHRC) and can be found at https://ghrc.nsstc.nasa.gov/home/field-campaigns.

Table 1.3. NASA physical-validation field deployment efforts. Partners indicated in the first column [FMI- Finnish Meteorological Administration, UH- University of Helsinki; DOE- U.S. Department of Energy; ECCC- Environment Climate Change Canada]. HIWRAP= High Altitude Imaging Wind and Rain Airborne Profiler, EXRAD- ER-2 X-band Radar, CRS- Cloud Remote Sensing radar, CoSMIR- Conical Scanning Millimeter Imaging Radiometer, AMPR- Advanced Microwave Precipitation Radiometer, DoW- Doppler on Wheels, CPL- Cloud Physics Lidar, AirMSPI- Airborne Multi-angle Spectro Polarimetric Imager, eMAS- extended MODIS Airborne Simulator. Also see Skofronick-Jackson et al., 2018, (their Table 4).

Field Campaign (Partners)	Description
LPVEX 2010 (NASA, FMI, UH)	Light Precipitation Validation Experiment. High latitude cold rain over ocean and continental land surfaces. U. Wyoming King Air microphysics aircraft also carrying U. Wyoming W-band radar. FMI/UH C-band polarimetric radars, MRRs, radiometers, rawinsonde, snow video imager, disdrometer and rain gauge network.
MC3E 2011 NASA, DOE	Mid-latitude Continental Convective Clouds Experiment. Warm-season mid-latitude convective and stratiform precipitation. NASA ER-2 high altitude aircraft carrying HIWRAP Ka/Ku band radar, AMPR 10-85 GHz radiometer, UND Citation aircraft with microphysics suite, multi-frequency polarimetric radar network including NASA NPOL and DOE X/C-band radars, MRRs, dense rain gauge and disdrometer networks, high temporal resolution rawinsonde..
GCPEX 2012 (NASA, ECCC)	GPM Cold Season Precipitation Experiment. Mid-latitude synoptic and lake-effect snow. NASA DC-8 aircraft carrying 50-183 GHz CoSMIR radiometer, APR-2 Ka/Ku band radar. UND Citation microphysics aircraft, NRC C580 microphysics aircraft and W-band radar, C-band dual-pol radar, NASA D3R radar, MRR, Pluvio snow gauge and PIP network, rawinsonde.
IFloodS 2013 (NASA, U. Iowa)	Iowa Floods Studies. Warm-season mid-latitude mesoscale precipitation events and hydrologic validation. NASA NPOL and D3R radars, U. Iowa X-band radars, extensive gauge and disdrometer networks, soil moisture network.
IPHEx 2014 (NASA, Duke U.)	Integrated Precipitation and Hydrology Experiment. Warm-season orographic precipitation and hydrologic validation, coastal oceanic precipitation. NASA ER-2 carrying EXRAD, HIWRAP and CRS radars (X/Ka/Ku/W band), AMPR (10-85 GHz) and CoSMIR (50-183 GHz) radiometer suite, NASA NPOL and D3R radars, MRRs, ACHIEVE W-band radar, extensive disdrometer and rain gauge networks.
OLYMPEX 2015/16 (NASA, U. Washington)	Olympic Mountains Experiment. Cold season orographic and oceanic rainfall and snow; integrated hydrologic validation. NASA ER-2 carrying EXRAD, HIWRAP and CRS radars (X/Ku/Ka/W bands), AMPR (10-85 GHz) radiometer, AirMSPI polarimeter, eMAS VIS/IR imager, CPL backscatter lidar; NASA DC-8 carrying APR-3 (Ku/Ka/W-bands) radar, CoSMIR radiometer (50-183 GHz), MASC radiometer (118, 183 GHz) and dropsondes. NASA NPOL and D3R radars, NSF DOW radar, ECCC X-band radar, MRRs, PIPs, extensive rain gauge and disdrometer network, high temporal resolution rawinsondes.

In addition to the larger campaigns mentioned in Table 1.3, the NASA GV effort has deployed instrumentation in several international-led campaigns, most recently the International Collaborative Experiment–PyeongChang Olympics and Paralympics Experiment 2018 (ICE-POP 2018) led by the Korean Meteorological Administration to study heavy orographic snow.

4.2.4 Validation of the GPM IMERG Product

The NASA GV team conducts routine verification of IMERG Early (E), Late (L) and Final (F) products. Accordingly, herein we provide a few examples of analysis types routinely conducted for two geographic regions (Korea and CONUS) and for one extreme event, Hurricane Florence. Because IMERG is such a popular product, many other examples of IMERG validation and analysis are available in the broader community for different areas of the world (e.g., Tang et al., 2015, Tan et al., 2017a, Desfuli et al., 2017; O et al., 2017, Rios-Gaona et al. 2017, O and Kirsetter, 2018).
IMERG can be briefly described as a global gridded precipitation product that unifies microwave measurements from the GPM *network* of satellites with geostationary VIS/IR sensors sampling at higher temporal and spatial resolution (cf. Huffman et al., 2018). IMERG covers latitudes of ±60^o with high resolution 0.1^o spatial and 30 minute temporal sampling. To accommodate various user requirements for data latency and accuracy, the IMERG is generated in the form of near-real-time (IMERG-E, and IMERG-L) and post-real-time research data that also incorporates a rain gauge-bias correction (IMERG-F). IMERG has undergone several episodes of development with many continuing improvements; here we examine Version-5b (V5b). Multi-scale validation of IMERG products for many versions and regions is essential to improving the product and its applications.
GV datasets including the GV-MRMS L3 products for CONUS, and KMA Real-time Adjusted Radar-AWS Rain rate (RAD-RAR) hourly rain accumulations (Table 1.2) are used to conduct a

variety of comparisons with IMERG. Due to differences in spatial and temporal resolution among products, the validation is carried out using an approach that matches and temporally resamples specific GV and IMERG data to common grids (nominally 0.1°, and either 30 minutes for GV-MRMS, or 1-hour for RAD-RAR); missing data are excluded. Standard statistical metrics such as Correlation Coefficient (CC), Relative Bias (Bias), NMAE, NRMSE are used to quantitatively compare the performance of IMERG products. Comparisons between IMERG and the ground reference are conducted for individual extreme events (e.g., hurricanes), regional to continental spatial, and diurnal to multi-annual temporal scales. Common approaches using probability density and cumulative density functions (PDF, CDF, respectively) for rain occurrence and volume, scatter density plots, time series of daily rainfall, and instantaneous hourly rainfall are routinely produced. To evaluate precipitation detection capability, three widely applied categorical statistical metrics are also employed in the analyses: Probability of Detection (POD), False Alarm Ratio (FAR) and Heidke Skill Score (HSS). Contributions to errors are also evaluated as a function of the estimator type (e.g., IR or passive microwave), and fraction of contribution to the relative bias is examined by partitioning error into hit, miss and false alarm biases. A full collection of IMERG analyses with updates as new data are received can be viewed at the NASA GPM-GV website https://gpm-gv.gsfc.nasa.gov/.

4.2.4.1 Examples of IMERG validation over South Korea

Validation of IMERG using Korean RAD-RAR data is performed over the latitude/longitude box region enclosed by [124.5 °E-130.5 °E, 32.5 °N-39 °N]. Results herein focus on a commonly available period from March 2014 to October 2017. All data are resampled to 0.1°/1-h resolutions. The NASA GV team routinely updates results at: https://wallops-prf.gsfc.nasa.gov/KoreanQPE.V05/index.html.

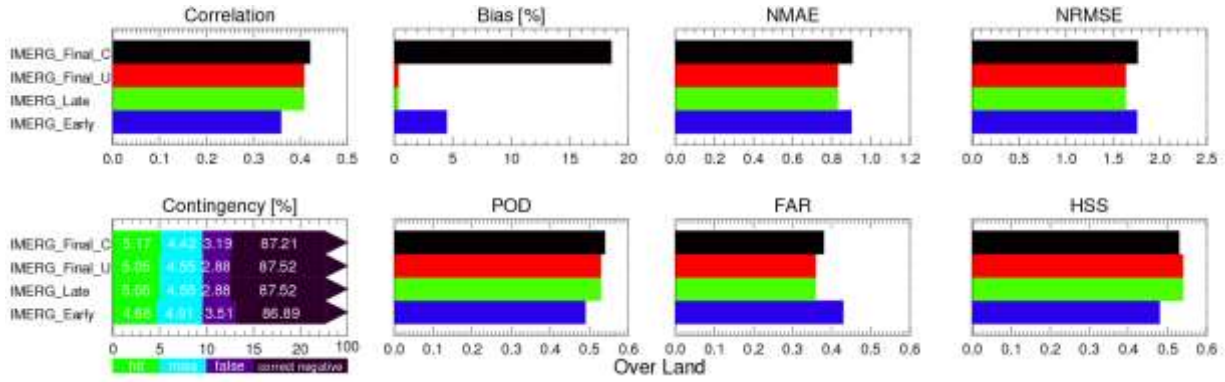

Figure 13. March 2014 to October 2017 V5b IMERG vs. RAD-RAR statistics for Early (IMERG_E), Late (IMERG_L), Final without gauge adjustment (IMERG_F_U), and Final with gauge adjustment (IMERG_F_G). Top panels: Pearson correlation coefficient(Correlation), Bias (%), NMAE, and NRMSE. Bottom: contigency scores for hits (green), misses (light blue), false alarms (purple), and correct negatives (black). POD, FAR and HSS are also indicated.

Categorical statistics (Figure 13) suggest that IMERG products compare reasonably well with the RAD-RAR over the region of South Korea as a whole. IMERG-F appears to be in the best agreement with the RAD-RAR in terms of correlation and POD. The expected improvement in skill between the IMERG-E and L products is also evident, likely due to the inclusion of more microwave data and forward/backward morphing in IMERG-L. It is interesting to note that IMERG-E and IMERGL outperform the gauge bias-corrected IMERG-F, at least in terms of relative bias and uncertainty. Indeed, Figure 14 suggests that monthly gauge-adjustments in the IMERG-F enhance disagreement with the RAD-RAR, increasing overestimation of precipitation rates- especially along the orography and coastline of the eastern Korean Peninsula. This is further demonstrated in Figure 15 when the

bias errors are decomposed into hit, miss, and false precipitation errors. Figure 15 suggests that the IMERG hit-bias is the primary driver of the bias error pattern for the period examined.

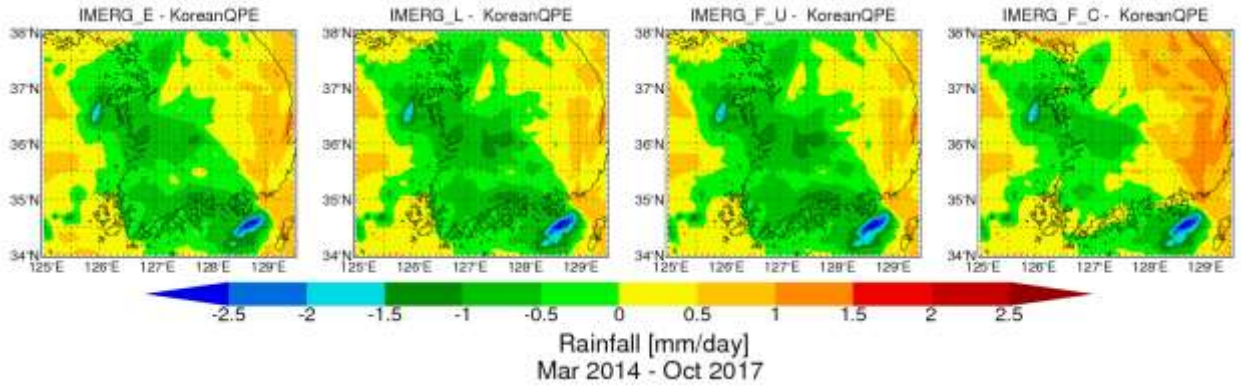

Figure 14. Difference in daily rainfall between RAD-RAR and IMERG-E, L, F-U and F-C, products.

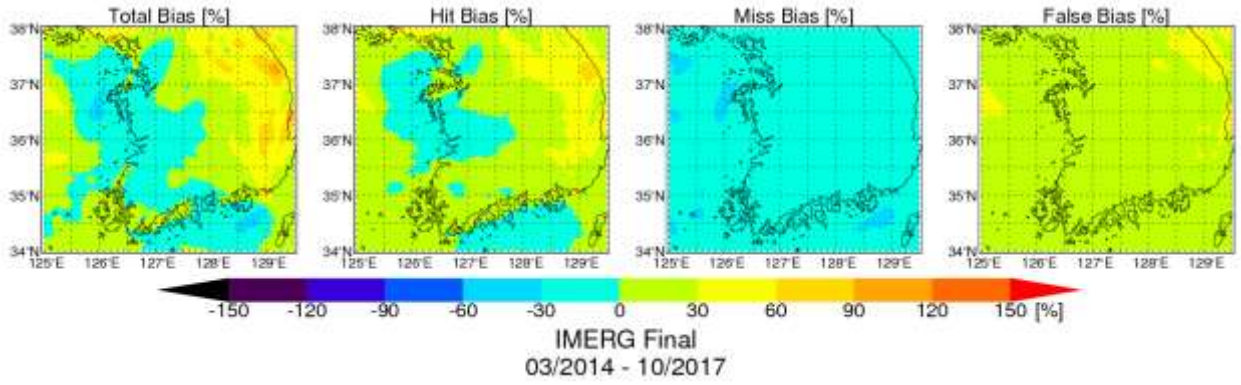

Figure 15. Error components of IMERG-F V5b Final for March 2014 – October 2017 broken down by total bias (E), hit bias (H), biases due to missing precipitation (M), and false precipitation (F).

4.2.4.2 Select Examples of IMERG validation over CONUS

For verification studies of IMERG over CONUS we use half-hourly gauge-adjusted GV-MRMS rain accumulations at 0.01° resolution (e.g., Tan et al, 2017a, O and Kirstetter, 2017). The comparisons are conducted at various spatial and temporal scales with respect to different precipitation intensities, and filtered with GV-MRMS radar quality index (RQI) thresholds as needed. As a first example, consider the scatter-density plots of Figure 16. These plots demonstrate both the general performance of IMERG vs. GV-MRMS, but also enable tracking of performance between versions. Figure 16 demonstrates the improved performance of IMERG-L in V5b relative to V4 and GV-MRMS. The discretization of IMERG values in V4 is associated with the presence of underlying rain rate modes that existed in V4 of the the passive microwave GPROF estimates. This issue was fixed in GPROF V5. Figure 16 suggests IMERG V5 exhibits a slightly high bias for rain rate values greater than ~1 mm hr^{-1} when considered at CONUS scale. Figure 17 suggests that the bias indicated in Figure 16 may be due to enhanced false-alarms over the central U.S. combined with hit-bias reflecting IMERG sensitivity to underlying passive microwave estimates observed over the central portions of the U.S. (e.g., Fig. 10).

Of great interest to the applications community is the relative performance of IMERG in extreme rain events. Accordingly, we provide an example here of GV-MRMS use for evaluating the performance of IMERG in estimating rain accumulations associated with the land-fall of Hurricane Florence. Florence made landfall near Wrightsville Beach, North Carolina (NC) on September 14, 2018 as a Category-1 hurricane on the Saffer-Simpson scale. However, Florence stalled along the Carolina

coastline just prior to and during its landfall, resulting in several days of excessive rain that occurred over a persistant storm surge- the combined effect being extensive and record-setting flooding.

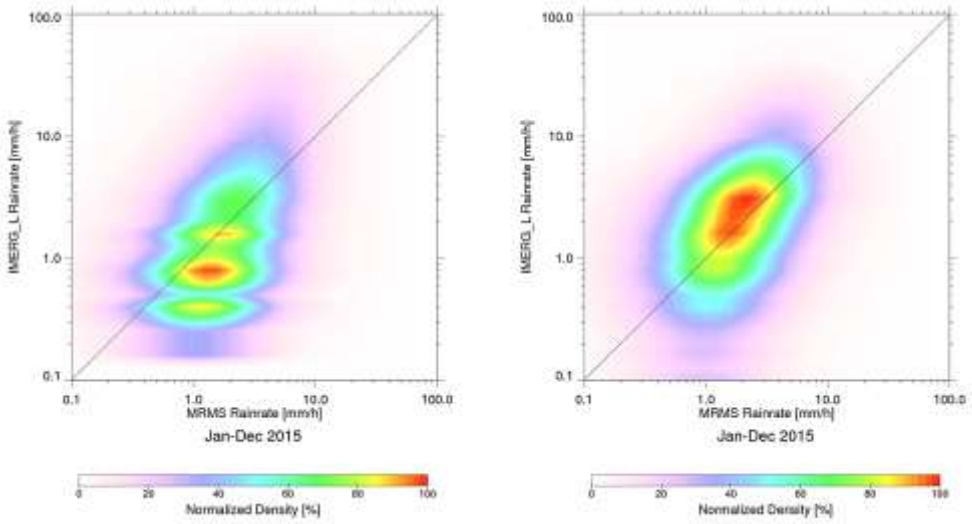

Figure 16. CONUS-wide comparisons of V04A (left) and V5b (right) IMERG-L 30 minute rain rates to GV-MRMS for the year of 2015.

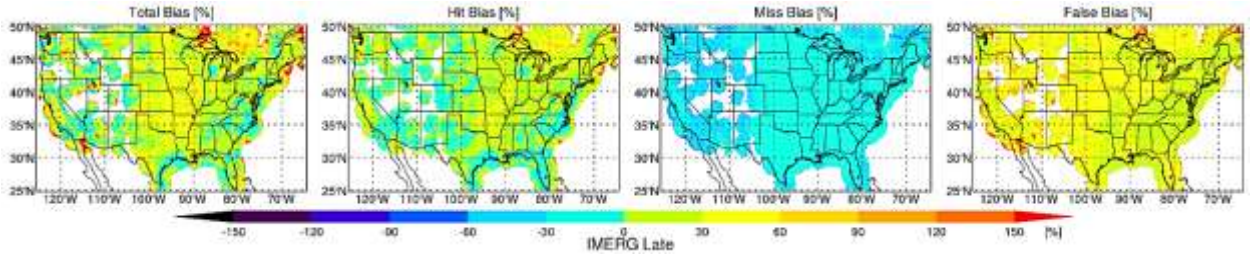

Figure 17. As in Fig. 14, but CONUS IMERG-L compared to GV-MRMS June 2014 – August 2017.

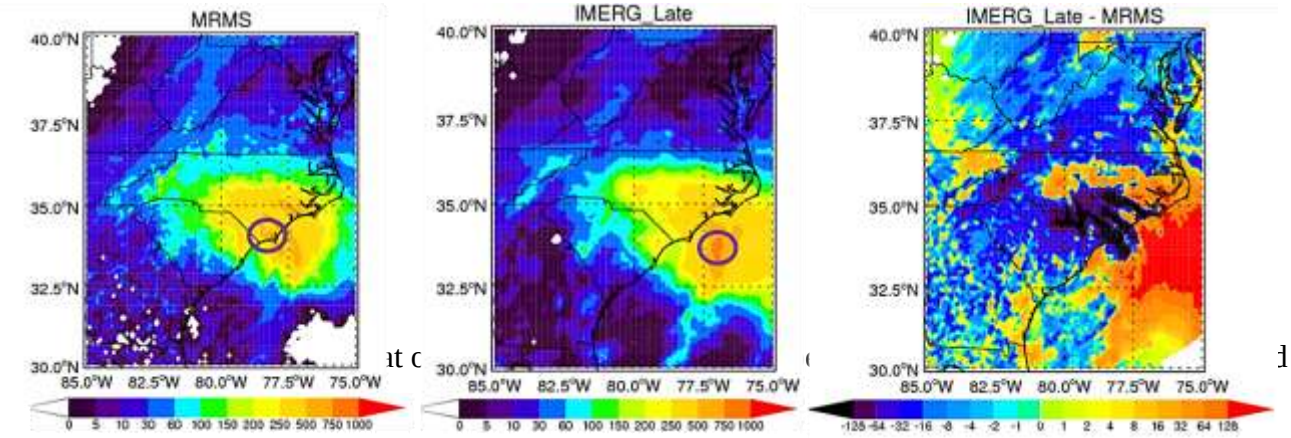

Figure 18. Hurricane Florence total rain accumulation (mm) for September 10 – 16, 2018. Totals for the GV-MRMS, IMERG-L, and the difference in accumulation between the two (MRMS-IMERG) are displayed in the left, center and right panels, respectively. The location of the maximum accumulations for GV-MRMS and IMERG are indicated by the dark circle.

900 mm, and more than 850 mm was measured at one gauge along the NC central coastline. An example of the GV-MRMS and IMERG-L product total rain accumulation for a seven-day period bracketing the period of heaviest rain over the Carolinas (10-17 September) is shown in Figure 18

together with a map of the difference in accumulation between GV-MRMS and IMERG. The GV-MRMS maximum accumulations are located in approximately the right locations relative to reported rain gauge maxima. The GV-MRMS maximum was 890 mm, close to that of gauge reports. In contrast, the IMERG-L maximum accumulation was located offshore at a value of 862 mm (~120 mm larger than the IMERG-E estimate, not shown). It is clear from the difference field in Figure 18 that the IMERG-L bias structure was affected by the bands of the hurricane and associated training precipitation features along those bands. IMERG estimated much lower rainfall than the GV MRMS in bands located over southern NC and larger amounts in a band located over northern NC and offshore (some of the apparent bias 150 km or more offshore may be the result of GV-MRMS radar estimates overshooting precipitation at distant ranges). Another interesting bias feature in the difference plot of Figure 18 is the prominant band of low bias long the foothills of the Appalachian Mountains. Here IMERG appears to have underestimated an orographically-forced component of the rainfall that was detected by GV-MRMS radars and gauges.

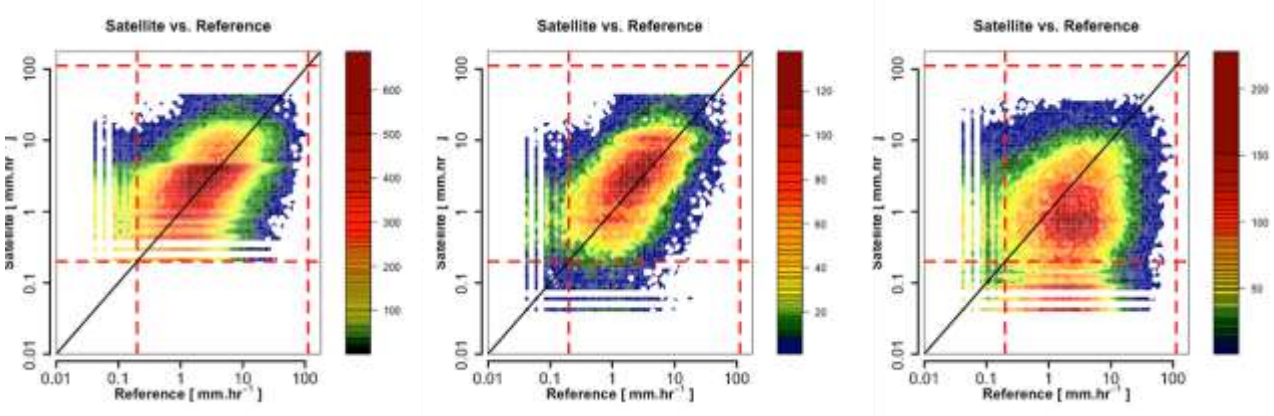

Figure 19. As in Figs. 6-7, but 30 minute rainrates for domain of Fig. 16 for IMERG "Precipcal" (left), HQPrecip (microwave; center), and IR (right) during Hurricane Florence.

Figure 19 focuses on the contribution of two primary rain estimators to the IMERG calibrated precipitation estimate for Florence ("Precipcal" variable in the data files). Here there is a tendency for the microwave estimates to be slightly positively biased, but even more clear is the tendency for IR estimates to be very low biased. The observed trend of low IR-bias for Florence is also consistent with that noted by our team for other hurricanes such as Harvey, Irma and Michael (not shown). Further decomposition of error components by estimator will likely illuminate shortcomings and potential pathways to improve IMERG.

4.2.5 Summary and Moving Forward

The NASA GV team has successfully constructed high-quality "bread and butter" tools such as the GV-MRMS and VN for accomplishing fundamental direct validation and forged international collaborations for analysis of precipitation datasets in a variety of regimes. The team developed multi-parameter radar and supporting gauge and disdrometer instrument infrastructue and a "home base" to operate instruments in a supersite. During the pre and post-launch GPM phases GV planned and executed numerous field campaigns deploying supporting instruments on the ground and in the air. These physical validation datasets provided data enabling confirmation of basic approaches to DSD retrieval, scattering impacts on higher radar and radiometer frequencies, and basic variability of rain and snow properties to include applications in cloud modeling. In the post-launch phase, the GV team has been able to demonstrate conformance of GPM core observatory measurements to L1SRs, and provided data and analysis for numerous other applications ranging from multiple scattering and hail detection, drop size distribution issues in convection, and falling snow measurement. Moving forward, GPM GV will continue to improve reference measurements of SWER for use in radiometer

and radar algorithm retrieval testing and verification. GV will work to improve measurements and representation in algorithms of light rain, conduct more refined studies and resolution of the impacts of non-uniform beam filling on multiple physical aspects of precipitation retrieval- especially in convection. Continuing emphasis will be placed on investigating orographic precipitation structure, variability, and environmental controls, especially as they pertain to the coupling of remote sensing and algorithm retrieval methodologies. A renewed emphasis will be placed on validation of IMERG products, especially in the context of integrated hydrologic validation.

References

Amitai, E., W. A. Petersen, X. Llort, and S. Vasilof, 2012: Multi-platform comparisons of rain intensity for extreme precipitation events. *IEEE Trans. on Geoscience and Remote Sensing*, **50,** 675-686

Battaglia, A., S. Tanelli, G. M. Heymsfield, and L/ Tian, 2014: The Dual Wavelength Ratio Knee: A Signature of Multiple Scattering in Airborne Ku–Ka Observations. *J. Appl. Meteor. Climatol*., **53**, 1790–1808

Battaglia A, Mroz K, Lang T, Tridon F, Tanelli S, Tian L, Heymsfield GM. 2016. Using a multiwavelength suite of microwave instruments to investigate the microphysical structure of deep convective core. *J. Geophys. Res.* **121** : 9356 - 9381. doi: 10.1002/2016JD025269

Bolen, S. and Chandrasekar, V. (2003) Methodology for aligning and comparing spaceborne radar and ground-based radar observations. *J. Atmos. Oceanic Tech*., **20**, 647–659, doi.org/10.1175/1520-0426(2003)20<647:MFAACS>2.0.CO;2.

Brandes, E. A., G. Zhang, and J. Vivekanandan, 2004: Drop size distribution retrieval with polarimetric radar: Model and application. *J. Appl. Meteor*., **43**, 461-475, doi:10.1175/1520-0450(2004)043<0461:DSDRWP>2.0.CO;2

Bringi, V.N., T. Tang, and V. Chandrasekar, 2004: Evaluation of a New Polarimetrically Based Z–R Relation. *J. Atmos. Oceanic Tech*., **21**, 612–623.

Bringi, V. N., M. Thurai, L. Tolstoy, W. A. Petersen, 2015: Estimation of spatial correlation of rain drop size distribution parameters and rain rate using NASA's S-band polarimetric radar and 2D-video disdrometer network: Two case studies from MC3E. *J. Hydromet*., 16, 1207-1221

Bukovcic, P., A. Ryzhkov, D. Zrnic, and G. Zhang, 2018: Polarimetric radar relations for quantification of snow based on disdrometer data. *J. Appl. Meteor. Climatol*., **57**, 103-121. doi: 10.1175/JAMC-D-17-0000-1.

Chandrasekar, V., and coauthors, 2008: Use of dual polarization radars for validation of spaceborne precipitation measurements: Rationale and opportunities. *Bull. Amer. Meteorol. Soc*., **89**, 1127-1145

Chase, R., and coauthors, 2018: Evaluation of triple-frequency radar retrieval of snowfall properties using coincident airborne in-situ observations during OLYMPEX. *Geophys. Res. Lett*., in press. doi:10.1029/2018GL077997.

Chen, S., and coauthors, 2016: Comparison of snowfall estimates from the NASA CloudSat Cloud Profiling Radar and NOAA/NSSL Multi-Radar Multi-Sensor System. *J. Hydrology*, **541**, 862–872, doi.org/10.1016/j.jhydrol.2016.07.047

Chen, H., V. Chandrasekar, and R. Bechini, 2017: An Improved Dual-Polarization Radar Rainfall Algorithm (DROPS2.0): Application in NASA IFloodS Field Campaign. *J. Hydrometeor*., **18**, 917-937., doi: 10.1175/JHM-D-16-0124.1

Cifelli, R. C., V. Chandrasekar, S. Lim, P. C. Kennedy, Y. Wang, and S. A. Rutledge, 2011: A new dual-polarization radar rainfall algorithm: Application in Colorado precipitation events. *J. Atmos. Oceanic Technol*., **28**, 352–364, doi:10.1175/2010JTECHA1488.1.

Colle BA, Naeger AR, Molthan A. 2017. Structure and Evolution of a Warm Frontal Precipitation Band during the GPM Cold Season Precipitation Experiment (GCPEx). Mon. Wea. Rev. **145**, 473 - 493. DOI: 10.1175/MWR-D-16-0072.1

Dezfuli, A. K., C. M. Ichoku, G. J. Huffman, K. I. Mohr, J. S. Selker, N. van de Giesen, R. Hochreutener, and F. O. Annor, 2017: Validation of IMERG Precipitation in Africa. *J. Hydrometeor*., **18**, 2817-2825. doi.org/10.1175/JHM-D-17-0139.1.

Dolan, B., and S. A. Rutledge, 2009: A theory-based hydrometeor identification algorithm for x-band polarimetric radars. *J. Atmos. Oceanic Tech*., **26**, 2071- 2088, doi.org/10.1175/2009JTECHA1208.1.

Gatlin, P., V. N. Bringi, M. Thurai, W. Petersen, D. B. Wolff, A. Tokay, L. D. Carey, M. Wingo, 2015: Searching for large raindrops: A global summary of two-dimensional video disdrometer observations. *J. Appl. Meteorol. Clim.,* **54**, 1059-1069

Gerlach, J., and W. A. Petersen, 2011: NPOL: The NASA transportable S-band dual-polarimetric Radar. Antenna system upgrades, performance and deployment during MC3E. *Preprints*, 35th Conf. on Radar Meteorology, Amer. Meteorol. Soc., 25-30 September, 2011, Pittsburgh, PA, USA.

Grecu M, Olson WS, Munchak SJ, Ringerud S, Liao L, Haddad Z, Kelley BL, McLaughlin SF. 2016. The GPM Combined Algorithm. *J. Atmos. Oceanic Technol.* 33 : 2225 - 2245. DOI: 10.1175/JTECH-D-16-0019.1

Heymsfield, G. M., L, Tian, L. Li, M. McLinden, J. I. Cervantes, 2013: Airborne Radar Observations of Severe Hailstorms: Implications for Future Spaceborne Radar. *J. Appl. Meteor. Climatol*., **52**, 1851–1867. doi.org/10.1175/JAMC-D-12-0144.1

Hou, A. Y., and Coauthors, 2014: The Global Precipitation Measurements Mission. *Bull. Amer. Meteor. Soc.*, **95**, 701-722, doi:10.1175/BAMS-D-13-00164.1.

Houze, R. A., L. McMurdie, W. A. Petersen, and coauthors:, 2017: The Olympic Mountains Experiment (OLYMPEX). *Bull. Amer. Meteorol. Soc*., DOI:10.1175/BAMS-D-16-0182.1

Huang, G., V. N. Bringi, D. Moisseev, W. Petersen, L. Bliven, D. Hudak, 2015: Use of 2D-Video Disdrometer to Derive Mean Density-Size and Z_e-SR Relations: Four Snow Cases from the Light Precipitation Validation Experiment. *Atmos. Res*., **153**, 34-48

Huffman, G. J., D. T. Bolvin, D. Braithwaite, K. Hsu, R. Joyce, C. Kidd, E. Nelkin, S. Sorooshian, J. Tan, and P. Xie, 2018: NASA Global Precipitation Measurement (GPM) Integrated Multi-Satellite Retrievals for GPM (IMERG) Algorithm Theoretical Basis Doc. version 5.2. NASA GSFC, 30 pp. See: https://pmm.nasa.gov/sites/default/files/document_files/IMERG_ATBD_V5.2.pdf.

Iguchi T, and coauthors, 2014: WRF–SBM Simulations of Melting-Layer Structure in Mixed-Phase: Precipitation Events Observed during LPVEx. *J. Appl. Meteor. Climatol.* **53** : 2710 - 2731. DOI: 10.1175/JAMC-D-13-0334.1

Jensen, M., W. A. Petersen and coauthors, 2016: The Midlatitude Continental Convective Clouds Experiment (MC3E). *Bull. Amer. Meteorol. Soc*., **97**, 1667-1686. DOI:10.1175/BAMS-D-14-00228.1

Kidd, C., J. Tan, P. Kirstetter, W. Petersen, 2018: Validation of the Version 05 precipitation products from the GPM Core Observatory and constellation satellite sensors. *Q. J. R. Meteorol. Soc*., **144**, 313–328, https://doi.org/10.1002/qj.3175.

Kirchengast, G., Kabas, T., Leuprecht, A., Bichler, C., and Truhetz, H. (2014). WegenerNet – A pioneering high-resolution network for monitoring weather and climate. *Bull. Amer. Meteor. Soc*., **95**:227–242. doi:10.1175/BAMS-D-11-00161.1

Kirstetter, P., and coauthors, 2012: Toward a framework for systematic error modeling of spaceborne precipitation radar with NOAA/NSSL ground radar-based National Mosaic QPE. *J. Hydrometeorol*., **13**, 1285-1300, doi:10.1175/JHM-D-11-0139.1.

Kirstetter, P.E., Y. Hong, J. J. Gourley, Q. Cao, M. Schwaller, and W. Petersen, 2014: A research framework to bridge from the Global Precipitation Measurement mission core satellite to the constellation sensors using ground radar-based National Mosaic QPE. In L. Venkataraman, Remote Sensing of the Terrestrial Water Cycle. AGU books Geophysical Monograph Series, Chapman monograph on remote sensing. John Wiley & Sons Inc. ISBN: 1118872037.

Kirstetter, P.-E., J. J. Gourley, Y. Hong, J. Zhang, S. Moazamigoodarzi, C. Langston, and A. Arthur, 2015: Probabilistic precipitation rate estimates with ground-based radar networks, *Water Resour. Res*., **51**, 1422–1442, doi:10.1002/2014WR015672

Kirstetter, P.E., Y. Hong, J.J. Gourley, M. Schwaller, W. Petersen and Q. Cao, 2015: Impact of sub-pixel rainfall variability on spaceborne precipitation estimation: evaluating the TRMM 2A25 product. *Q. Journal of the Royal Met. Soc.*, **141**, 953–966. doi:10.1002/qj.2416.

Kneifel S, von Lerber A, Tiira J, Moisseev D, Kollias P, Leinonen J. 2015. Observed relations between snowfall microphysics and triple-frequency radar measurements: Triple frequency signatures of snowfall. *J. Geophys. Res*. 120 : 6034 – 6055. DOI: 10.1002/2015JD023156

Kummerow, C.D., and coauthors, 2015: The evolution of the Goddard profiling algorithm to a fully parametric scheme. *J. Atmos. Oceanic Tech.*, **32**, 2265–2280, doi.org/10.1175/JTECH-D-15-0039.1

Lang, S., W. Tao, J. Chern, D. Wu, and X. Li, 2014: Benefits of a 4th Ice Class in the Simulated Radar Reflectivities of Convective Systems using a Bulk Microphysics Scheme. *J. Atmos. Sci*. doi:10.1175/JAS-D-13-0330.1.

Leinonen, J., and coauthors, 2018: Retrieval of snowflake microphysical propertiers from multi-frequency radar observations. *Atmos. Meas. Tech. Discuss*., in press. doi.org/10.5194/amt-2018-73.

Leppert, K. D., and D. J. Cecil, 2015: Signatures of Hydrometeor Species from Airborne Passive Microwave Data for Frequencies 10–183 GHz. *J. Appl. Meteor. Climatol.*, **54**, 1313-1334, doi:10.1175/JAMC-D-14-0145.1.

Liao, L., R. Meneghini, and A. Tokay, 2014: Uncertainties of GPM DPR Rain Estimates Caused by DSD Parameterizations. *J. Appl. Meteor. Climatol.*, **53**, 2524-2537, doi:10.1175/JAMC-D-14-0003.1.

Liao, L., R. Meneghini, A. Tokay, and L. F. Bliven, 2016: Retrieval of snow properties fro Ku- and Ka-Band dual-frequency radar. *J. Appl. Meteor. Climatol*, **55**, 1845-1858. doi: 10.1175/JAMC-D-15-0355.1.

Louf., V., and coauthors, 2018: An integrated approach to weather radar calibration and monitoring using ground clutter and satellite comparisons. *J. Atmos. Oceanic Tech*., in press.

Marks, D., and D. B. Wolff, 2011: Quality control and calibration of the dual-polarization radar at Kwajalein, RMI. *J. Atmos. Oceanic Tech.*, **28**, 181-196, doi.org/10.1175/2010JTECHA1462.1

Marks, D., and coauthors, 2017: Evaluation of S-Band radar rain rate retrieval algorithms and precipitation variability over a dense rain gauge network. Preprints, AMS 38th Conference on Radar Meteorology, August 27 – September 1, Chicago, Illinois, USA.

Matsui, T., and Coauthors, 2013: GPM satellite simulator over ground validation sites. *Bull. Amer. Meteor. Soc*., **94**, 1653-1660, doi:10.1175/BAMS-D-12-00160.1.

Molthan, A., and W. A. Petersen, 2011: Incorporating Ice Crystal Scattering Databases in the Simulation of Millimeter Wavelength Radar Reflectivity, *J. Atmos. Ocean Tech*., **26**, 2257-2269.

Newman, A., Kucera, P. and Bliven, L. (2009) Presenting the Snowflake Video Imager (SVI). *J. Atmos. Oceanic Tech*., **26**, 167–179, doi.org/10.1175/2008JTECHA1148.1

O, S., U. Foelsche, G. Kirchengast, J, Fuchsberger, J. Tan, and W. A. Petersen, 2017: Evaluation of GPM IMERG Early, Late, and Final rainfall estimates using WegenerNet gauge data in southeastern Austria. *Hydrol. Earth Syst. Sci*., **21**, 6559–6572, 2017. doi.org/10.5194/hess-21-6559-2017

O, S., and P. Kirstetter, 2018: Evaluation of diurnal variation of GPM IMERG-derived summer precipitation over the contiguous US using MRMS data. *Q. J. R. Meteorol*. Soc., **144**, 270-281, doi.org/10.1002/qj.3218k.

Olson, W. S., and Coauthors, 2016: The Microwave Radiative Properties of Falling Snow Derived from Nonspherical Ice Particle Models. Part II: Initial Testing Using Radar, Radiometer and In Situ Observations. *J. Appl. Meteor. Climatol.*, **55**, 709-722, doi:10.1175/JAMC-D-15-0131.1.

Petkovic, V., and C. Kummerow, 2017: Understanding the sources of satellite passive microwave rainfall retrieval systematic errors over land. *J. Appl. Meteor. Climatol.*,**56**, 597-614, doi.org/10.1175/JAMC-D-16-0174.1.

Petersen, W. A. and coauthors, 2013: Appendix J. Bias and Random Error Estimates Using Pre-GPM Satellite Products and Ground Validation Rain Rate Estimates, in GPM Science Implementation Plan, Ed. A. Hou, NASA GSFC Technical Document, available at: https://pmm.nasa.gov/resources/documents/GPM.

Petersen, W.A., R.A. Houze, L. McMurdie, J. Zagrodnik, S. Tanelli, J. Lundquist, J. Wurmann, 2016: The Olympic Mountains Experiment (OLMPEX): From Ocean to Summit. Meteorol. Tech. International., Vol. Sept. 2016, pp 22-26

Petersen, W. A., P. N. Gatlin, D. B. Wolff, A. Tokay, and M. Grecu, 2018: A Radar-based evaluation of GPM retrievals of the rain drop size distribution. 10th European Conference on Radar in Meteorology and Hydrology (ERAD 2018) : 1-6 July 2018, Ede-Wageningen, The Netherlands. doi: 10.18174/454537

Pippitt, J., D. B. Wolff, W. A. Petersen, and D. Marks, 2015: Data and operational processing for NASA's GPM ground validation program. 37th Conf. on Radar Meteorology, Norman, OK, Amer. Meteor. Soc., [Available online at https://ams.confex.com/ams/37RADAR/webprogram/Paper275627.html].

Rios Gaona, M. F., and coauthors, 2017: Evaluation of rainfall products derived from satellites and microwave links for The Netherlands, *IEEE Trans. Geosci. Remote Sensing*, 55, 6849-6859, doi:10.1109/TGRS.2017.2735439

Schwaller, M. R., and K. R. Morris, 2011: A Ground Validation Network for the Global Precipitation Measurement Mission. *J. Atmos. Oceanic Technol*., **28**, 301–319, doi:10.1175/2010JTECHA1403.1

Seo, B.-C., and coauthors, 2018. Comprehensive evaluation of the IFloodS radar-rainfall products for hydrologic applications. *J. Hydrometeor*., in press.

Seto, S. and Iguchi, T. (2015) Intercomparison of attenuation correction methods for the GPM dual-frequency precipitation radar. *J. Atmos. Oceanic Tech*., **32**, 915–926, doi.org/10.1175/JTECH-D-14-00065.1.

Shi, R. and Coauthors, 2010: WRF Simulations of the 20-22 January 2007 Snow Events over Eastern Canada: Comparison with in-situ and Satellite Observations. *J. Appl. Meteor. Climatol*., **49**, 2246-2266, doi:10.1175/2010JAMC2282.1.

Suk, M-K, K-H Chang, J-W Cha, K-E Kim, 2013: Operational real-time adjustment of radar rainfall estimation over the South Korea region *J. Meteorol. Soc.Japan*, **91**, 545-554. doi:10.2151/jmsj.2013-409

Skofronick-Jackson, G., B. T. Johnson, S. J. Munchak, 2013: Detection Thresholds of Falling Snow from Satellite-Borne Active and Passive Sensors. IEEE Transactions on Geoscience and Remote Sensing, **51**, 4177-4189, doi:10.1109/TGRS.2012.2227763

Skofronick-Jackson, G., and Coauthors, 2015: Global Precipitation Measurement Cold Season Precipitation Experiment (GCPEx): For Measurement Sake Let it Snow. *Bull. Amer. Meteor. Soc.*, **96**, 1719–1741, doi:10.1175/BAMS-D-13-00262.1

Skofronick-Jackson, G., W. A. Petersen, and coauthors, 2017: The Global Precipitation Measurement (GPM) Mission for Science and Society. *Bull. Amer. Meteorol. Soc*., **98**, 1675-1699. doi:10.1175/BAMS-D-15-00306.1

Skofronick-Jackson, G., D. Kirschbaum, W. Petersen, G. Huffman, C. Kidd, E. Stocker, R. Kakar, 2018: GPM scientific achievements and societal contributions: reviewing three years of advanced rain and snow measurements. *Q. J. R. Met. Soc.*, in press.

Steiner, M., T. L. Bell, Y. Zhang, and E. F. Wood, 2003: Comparison of two methods for estimating the sampling-related uncertainty of satellite rainfall averages based on large radar dataset. *J. Climate*, **16**, 3759–3778, doi:10.1175/1520-0442(2003)016,3759: COTMFE.2.0.CO;2.

Tan, B.-Z, W. A. Petersen**,** and A. Tokay, 2016: A Novel Approach to Identify Sources of Errors in IMERG for GPM Ground Validation. *J. Hydrometeorol*., **17**, 2477-2491.

Tan, B.-Z., W. A. Petersen, P. Kirstetter, and Y. Tian, 2017a: Performance of IMERG as a Function of Spatiotemporal Scale. *J. Hydromet*, 18, 307-319, doi: 10.1175/JHM-D-16-0174.1.

Tan, B.-Z., W. A. Petersen, and coauthors, 2017b: On the evaluation of GPM Ku and GPROF against three dense gauge networks. *J. Hydrometeorol.,* **19**, 517–532, doi:10.1175/JHM-D-17-0174.1.

Tang, G., and coauthors, 2015: Statistical and hydrological comparisons between TRMM and GPM Level-3 products over a midlatitude basin: Is day-1 IMERG a good successor for TMPA 3B42V7? *J. Hydrometeor*., **17**, 121-137, doi: 10.1175/JHM-D-15-0059.1

Tao, W.-K., D. Wu, T. Matsui, C. Peters-Lidard, S. Lang, A. Hou, M. Reinecker, and W. A. Petersen, 2013. The diurnal variation of precipitation during MC3E: A modeling study. *J. Geophys. Res*., **118**, 7199–7218, doi:10.1002/jgrd.50410/asset/jgrd50410.

Tao, W.-K, and Coauthors, 2014: The Goddard Cumulus Ensemble model (GCE): Improvements and applications for studying precipitation processes. *Atmos. Res.*, **143**, 392-424, doi:10.1016/j.atmosres.2014.03.005.

Thurai, M., V. N. Bringi, L. D. Carey, P. Gatlin, E. Schultz, and W. A. Petersen, 2012: Estimating the accuracy of polarimetric radar-based retrievals of drop size distribution parameters and rain rate: An application of error variance separation using radar-derived spatial correlations. *J. Hydrometeorol*, **13**, 1066–1079.

Thurai, M., P. N. Gatlin, V. N. Bringi, W. Petersen, P. Kennedy, B. Notaros, and L. D. Carey, 2017: Towards Completing the Rain Drop Size Spectrum: Case Studies Involving 2D-Video Disdrometer, Droplet Spectrometer, and Polarimetric Radar Measurements. *J. Appl. Meteor. Soc*., **56**, 877-896. doi: 10.1175/JAMC-D-16-0304.1.

Tokay, A., L. D'Adderio, F. Porcu, D. Wolff, and W. Petersen, 2017: A Field Study of Footprint-Scale Variability of Raindrop Size Distribution. *J. Hydrometeor*., **16**, 1855-1868, doi:10.1175/JHM-D-15-0159.1.

Tokay, A., and coauthors, 2018: Development and evaluation of the raindrop size distribution parameters for the NASA Global Precipitation Measurement Mission Ground Validation Program. *J. Atmos. Oceanic Tech*., in review.

Vega, M., Chandrasekar, V., Carswell, J., Beauchamp, R.M., Schwaller, M.R. and Nguyen, C.M., 2014: Salient features of the dual-frequency, dual-polarized, Doppler radar for remote sensing of precipitation. *Radio Science*, **49**, 1087–1105, doi.org/10.1002/2014RS005529

von Lerber, A., D. Moisseev, D. Marks, W. Petersen, A. Harri, V. Chandrasekar, 2018: Validation of satellite-based snowfall products by using a combination of weather radar and surface observations. *J. Appl. Meteorol. and Clim*., **57**, 797-820, doi.org/10.1175/JAMC-D-17-0176.1.

Williams, C. R., V. N. Bringi, L. Carey, P. Gatlin, Z. S. Haddad, S. J. Munchak, W. A. Petersen, R. Meneghini, S. W. Nesbitt, S. Tanelli, A. Tokay, M. Thurai, A. Wilson, and D. B. Wolff, 2014: Describing the shape of raindrop size distributions using uncorrelated raindrop mass spectrum parameters. *J. Appl. Meteorol. and Clim*., **53**, 1282-1296.

Wingo, S.-M., W. A. Petersen, C. S. Pabla, P. N. Gatlin, D. A. Marks, and D. B. Wolff, 2018: The System for Integrating Multi-platform data to Build the Atmospheric column (SIMBA) precipitation observation fusion framework. *J. Atmos. Oceanic Tech*., in press, https://doi.org/10.1175/JTECH-D-17-0187.1.

Wolff, David B., D. Marks, W. A. Petersen, 2015: General application of the Relative Calibration Adjustment (RCA) technique for monitoring and correcting radar reflectivity calibration. *J. Atmos. Oceanic Tech*., **32**, 496-506, doi:10.1175/JTECH-D-13-00185.1.

You, Y., N.-Y. Wang, R. Ferraro, and S. Rudlosky, 2016: Quantifying the Snowfall Detection Performance of the Global Precipitation Measurement (GPM) Microwave Imager Channels over Land. *J. Hydromet/.*,**17**, 1101-1117,doi.org/10.1175/JHM-D-16-0190.1.

Zagrodnick, J.P., McMurdie, L.A. and Houze, R.A., Jr, 2018: Stratiform precipitation processes in cyclones passing over a coastal mountain range. J. Atmos. Sciences, **75**, 983–1004, doi.org/10.1175/JAS-D-17-0168.1.

Zhang, J., and Coauthors, 2016: Multi-Radar Multi-Sensor (MRMS) Quantitative Precipitation Estimation: Initial Operating Capabilities. *Bull. Amer. Meteor. Soc.*, **97**, 621-638, doi:10.1175/BAMS-D-14-00174.1.